arXiv:1702.03412v1 [physics.flu-dyn] 11 Feb 2017

Optimal heat transfer enhancement in plane Couette flow

Shingo Motoki[1], Genta Kawahara[1]† and Masaki Shimizu[1]

[1]Graduate School of Engineering Science, Osaka University, 1-3 Machikaneyama, Toyonaka, Osaka 560–8531, Japan

(Received xx; revised xx; accepted xx)

Optimal heat transfer enhancement has been explored theoretically in plane Couette flow. The velocity field to be optimised is time-independent and incompressible, and temperature is determined in terms of the velocity as a solution to an advection-diffusion equation. The Prandtl number is set to unity, and consistent boundary conditions are imposed on the velocity and the temperature fields. The excess of a wall heat flux (or equivalently total scalar dissipation) over total energy dissipation is taken as an objective functional, and by using a variational method the Euler–Lagrange equations are derived, which are solved numerically to obtain the optimal states in the sense of maximisation of the functional. The laminar conductive field is an optimal state at low Reynolds number $Re \sim 10^0$. At higher Reynolds number $Re \sim 10^1$, however, the optimal state exhibits a streamwise-independent two-dimensional velocity field. The two-dimensional field consists of large-scale circulation rolls that play a role in heat transfer enhancement with respect to the conductive state as in thermal convection. A further increase of the Reynolds number leads to a three-dimensional optimal state at $Re \gtrsim 10^2$. In the three-dimensional velocity field there appear smaller-scale hierarchical quasi-streamwise vortex tubes near the walls in addition to the large-scale rolls. The streamwise vortices are tilted in the spanwise direction so that they may produce the anticyclonic vorticity antiparallel to the mean-shear vorticity, bringing about significant three-dimensionality. The isotherms wrapped around the tilted anticyclonic vortices undergo the cross-axial shear of the mean flow, so that the spacing of the wrapped isotherms is narrower and so the temperature gradient is steeper than those around a purely streamwise (two-dimensional) vortex tube, intensifying scalar dissipation and so a wall heat flux. Moreover, the tilted anticyclonic vortices induce the flow towards the wall to push low- (or high-) temperature fluids on the hot (or cold) wall, enhancing a wall heat flux. The optimised three-dimensional velocity fields achieve a much higher wall heat flux and much lower energy dissipation than those of plane Couette turbulence.

Key words: Mixing enhancement, variational methods

1. Introduction

The improvement of the performance of heat exchangers has always been crucial to efficient energy use. What is a flow field with the ability of the most efficient heat transfer? This may be a naive question in the development of flow control technique aimed at heat

† Email address for correspondence: kawahara@me.es.osaka-u.ac.jp

transfer enhancement. If we can find an optimal state in which heat transfer will be enhanced while suppressing energy loss, it will serve as the target of flow control.

For buoyancy-driven convection, Malkus (1954) raised a question of an upper limit to heat transfer and an optimal state realising it, and Howard (1963) formulated a variational problem to derive a theoretical upper bound on a heat flux. In the case of velocity fields satisfying the equation of continuity, Howard obtained the upper bound under the assumption that an optimal state has a single horizontal wavenumber, and subsequently Busse (1969) considered the same problem by using a multiple-boundary-layer approach to derive an asymptotic upper bound in a large-Rayleigh-number limit. Moreover, by using the same method, Busse (1970) found an upper bound on momentum transfer (or equivalently energy dissipation and so enstrophy), and conjectured an optimal velocity field consisting of hierarchical streamwise vortices in plane Couette flow with the aid of the so-called attached-eddy hypothesis (Townsend 1976). Later Doering and Constantin developed a new variational approach called 'the background method' and obtained a rigorous upper bound on energy dissipation in plane Couette flow (Doering & Constantin 1992, 1994) and a heat flux in Rayleigh–Bénard convection (Doering & Constantin 1996). The development of this method has triggered remarkable advancements in identification of optimal momentum transfer in shear flows (Nicodemus *et al.* 1997, 1998*a*,*b*; Plasting & Kerswell 2003) and optimal heat transfer in thermal convection (Kerswell 2001; Otero *et al.* 2002; Doering *et al.* 2006). Recently, Hassanzadeh *et al.* (2014) have reported optimal velocity fields for two-dimensional thermal convection without taking account of the Navier–Stokes equation as a constraint on fluid motion. They considered two-dimensional divergence-free velocity fields under one of the two types of constraints on velocity fields (fixed kinetic energy or fixed enstrophy). On the other hand, Sondak *et al.* (2015) have taken another approach to optimal heat transfer in the two-dimensional thermal convection, in which they optimised the aspect ratio of the two-dimensional domain for their steady solutions to the Navier–Stokes equation to achieve maximal heat transfer. To our knowledge, however, the velocity field for optimal heat transfer has not been determined in shear flows as yet.

Shear flow turbulence has an ability of significantly high heat transfer in comparison with laminar flow, but it results in friction loss as a consequence of simultaneous promotion of momentum transfer. This is well known as the similarity between heat and momentum transfer in engineering (Reynolds 1874; Chilton & Colburn 1934). Especially, when the Prandtl number, the ratio between thermal and momentum diffusivity, is close to unity, the heat and momentum transfer exhibit strong similarity (Dipprey & Sabersky 1963). Although one of the ultimate goals in turbulence control is more heat transfer and less friction, their achievement has been extremely difficult due to the similarity. Recently, however, control strategies to break the similarity have been proposed. Momentum transfer by viscous flow obeys the Navier–Stokes equation, whereas heat transfer is governed by the energy equation, i.e. an advection-diffusion equation for temperature. By applying the feedback control using the adjoint equations (Bewley *et al.* 2001; Kasagi *et al.* 2012) to heat transfer in turbulent channel flow with blowing and suction on the wall, Hasegawa & Kasagi (2011) and Yamamoto *et al.* (2013) have numerically achieved the dissimilarity even when the Prandtl number is equal to unity. Experimentally, several practicable passive or active control techniques have been developed using riblet (Sasamori *et al.* 2014), permeable wall (Suga *et al.* 2011), micro actuator and sensor (Kasagi *et al.* 2009), and so on. Hence, the accomplishment of dissimilar heat transfer enhancement by flow control might be expected in the near future.

The aim of this study is to find an optimal velocity field which will provide new insight

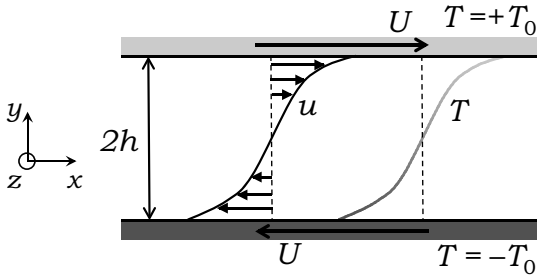

FIGURE 1. Configuration of the velocity and temperature fields.

into such flow control. We focus on optimal heat transfer in plane Couette flow. In this flow, the temperature and velocity field exhibit complete similarity in a laminar and conductive state, when a constant temperature difference is imposed between the two parallel walls. Furthermore, when the Prandtl number is set to unity, a turbulent state shows strong similarity between heat and momentum transfer. By taking the excess of the scalar dissipation (or equivalently, a total wall heat flux) over the energy dissipation as an objective functional, an optimal velocity field is determined by maximising the functional under the constraint of the continuity equation for the velocity and the advection-diffusion equation for the temperature.

This paper is organized as follows. In §2 we describe the flow configuration and the mathematical relation between scalar (or energy) dissipation and a wall heat (or momentum) flux, and then present the formulation of a variational problem. In §3, the details of numerical procedures and the parameter dependence of optimal velocity fields are explained. The spatial structures and the statistics of the optimal states are presented in §4, and the hierarchical structure of the optimal fields is discussed in §5. In §6 we discuss the significant effects of three-dimensional vortical structures on heat transfer enhancement in the optimal state. Section 7 is devoted to summary and discussion. Properties of the external body force to be added for the achievement of the optimal velocity field are described in Appendix A. An analytical interpretation of heat transfer intensification mechanisms through the spanwise inclination of a quasi-streamwise tubular vortex is given in Appendix B.

2. Mathematical formulation

2.1. *Flow configuration*

Figure 1 shows the configuration of the velocity and temperature fields. The flow is driven by the two parallel plates moving in the opposite directions at a constant speed U. The upper (or lower) wall surface is held at higher (or lower) constant temperature $+T_0$ (or $-T_0$). The coordinates, x, y and z (or x_1, x_2 and x_3), are used for the representation of the streamwise, the wall-normal and the spanwise directions, respectively, and their origin is on the midplane of the two plates separated by a distance $2h$. The corresponding components of the velocity $\boldsymbol{u}(x, y, z)$ are given by u, v and w (or u_1, u_2 and u_3) in the streamwise, the wall-normal and the spanwise directions, respectively.

Let us consider heat transfer in an incompressible time-independent velocity field fulfilling the continuity equation

$$\frac{\partial u_i}{\partial x_i} = 0. \tag{2.1}$$

We suppose that the temperature field $T(x, y, z)$ is determined as a solution to an

advection-diffusion equation

$$\frac{\partial}{\partial x_j}\left(u_j T\right) = \kappa \frac{\partial^2 T}{\partial x_j^2}, \tag{2.2}$$

where κ denotes thermal diffusivity. The velocity and temperature fields are supposed to be periodic in the x- and z-directions with the periods, L_x and L_z. The boundary conditions

$$u(y=\pm h) = \pm U, \quad v(y=\pm h) = w(y=\pm h) = 0; \quad T(y=\pm h) = \pm T_0 \tag{2.3}$$

are imposed on the walls.

2.2. *Scalar dissipation and heat flux*

We introduce the xz-average and the xyz-average given respectively by

$$\langle\cdot\rangle_{xz} = \frac{1}{L_x L_z}\int_0^{L_x}\int_0^{L_z} \cdot \,\mathrm{d}x\mathrm{d}z, \tag{2.4}$$

$$\langle\cdot\rangle_{xyz} = \frac{1}{2hL_x L_z}\int_0^{L_x}\int_{-h}^{h}\int_0^{L_z} \cdot \,\mathrm{d}x\mathrm{d}y\mathrm{d}z. \tag{2.5}$$

We take the xz-average of equation (2.2) to obtain

$$\frac{\mathrm{d}}{\mathrm{d}y}\langle vT\rangle_{xz} = \kappa\frac{\mathrm{d}^2}{\mathrm{d}y^2}\langle T\rangle_{xz}, \tag{2.6}$$

the y-integration of which gives us the total heat flux

$$\langle vT\rangle_{xz} - \kappa\frac{\mathrm{d}}{\mathrm{d}y}\langle T\rangle_{xz} = -\kappa\frac{\mathrm{d}}{\mathrm{d}y}\langle T\rangle_{xz}\left(y=-h\right) = \text{const.} \tag{2.7}$$

at any wall-normal position y. By further taking the average of equation (2.7) in the y-direction we have

$$\langle vT\rangle_{xyz} - \kappa\frac{T_0}{h} = -\kappa\frac{\mathrm{d}}{\mathrm{d}y}\langle T\rangle_{xz}\left(y=-h\right). \tag{2.8}$$

Now we decompose the temperature into a conductive state and a fluctuation about it as

$$T = T_0\frac{y}{h} + \theta. \tag{2.9}$$

The boundary conditions of the temperature fluctuation θ are

$$\theta(y=\pm h) = 0. \tag{2.10}$$

The substitution of decomposition (2.9) in (2.8) yields

$$\langle v\theta\rangle_{xyz} = -\kappa\frac{\mathrm{d}}{\mathrm{d}y}\langle\theta\rangle_{xz}\left(y=-h\right). \tag{2.11}$$

We substitute decomposition (2.9) for equation (2.2) to have

$$\frac{\partial}{\partial x_j}\left(u_j\theta\right) + v\frac{T_0}{h} = \kappa\frac{\partial^2\theta}{\partial x_j^2}. \tag{2.12}$$

The product of equation (2.12) with θ gives us

$$\frac{\partial}{\partial x_j}\left(u_j\frac{1}{2}\theta^2\right) + v\theta\frac{T_0}{h} = \kappa\frac{\partial}{\partial x_j}\left(\theta\frac{\partial\theta}{\partial x_j}\right) - \kappa\left(\frac{\partial\theta}{\partial x_j}\right)^2. \tag{2.13}$$

By further taking the xyz-average of equation (2.13) and taking into account boundary conditions (2.10), we obtain

$$\frac{T_0}{h}\langle v\theta\rangle_{xyz} = -\kappa\Big\langle|\nabla\theta|^2\Big\rangle_{xyz}, \tag{2.14}$$

where the right-hand side represents the dissipation of variance θ^2, hereafter referred to as 'scalar dissipation'. As a consequence, we have the expression of the wall heat flux

$$-\kappa\frac{\mathrm{d}}{\mathrm{d}y}\langle T\rangle_{xz}(y=+h) = -\kappa\frac{\mathrm{d}}{\mathrm{d}y}\langle T\rangle_{xz}(y=-h) = -\frac{\kappa h}{T_0}\Big\langle|\nabla\theta|^2\Big\rangle_{xyz} - \kappa\frac{T_0}{h}. \tag{2.15}$$

2.3. *Energy dissipation and momentum flux*

The steady motion of a viscous fluid is described by the Navier–Stokes equation

$$\frac{\partial}{\partial x_j}(u_iu_j) = -\frac{1}{\rho}\frac{\partial p}{\partial x_i} + \nu\frac{\partial^2 u_i}{\partial x_j^2} + f_i, \tag{2.16}$$

where p, ρ, ν and f_i are pressure, mass density, kinematic viscosity, and the i-th component of external body force per unit mass, respectively. The inner product of equation (2.16) with the velocity yields the local energy budget equation

$$\frac{\partial}{\partial x_j}\left(u_j\frac{1}{2}|\boldsymbol{u}|^2\right) = -\frac{1}{\rho}\frac{\partial}{\partial x_i}(pu_i) + \nu\frac{\partial}{\partial x_j}\left(u_i\frac{\partial u_i}{\partial x_j}\right) - \nu\left(\frac{\partial u_i}{\partial x_j}\right)^2 + u_if_i. \tag{2.17}$$

By taking the xyz-average of equation (2.17) and taking into account boundary conditions (2.3), we obtain the total energy budget equation

$$\frac{\nu}{2}\left[\frac{\mathrm{d}}{\mathrm{d}y}\langle u\rangle_{xz}(y=+h) + \frac{\mathrm{d}}{\mathrm{d}y}\langle u\rangle_{xz}(y=-h)\right] = \frac{\nu h}{U}\Big\langle|\nabla\boldsymbol{u}|^2\Big\rangle_{xyz} - \frac{h}{U}\langle u_if_i\rangle_{xyz}, \tag{2.18}$$

where we have supposed a null mean pressure gradient in the wall-parallel (x- and z-) directions. The left-hand side of equation (2.18) is mean wall shear stress, while the first and second terms in the right-hand side originate from energy dissipation and an energy input by the external force, respectively.

2.4. *Objective functional and Euler-Lagrange equation*

Let us now consider the optimisation problem of a functional to find an optimal state for the dissimilarity between momentum and heat transfer. As can be seen from equation (2.15) and (2.18), the wall heat flux corresponds to the total scalar dissipation, and the wall momentum flux (i.e. the skin friction) is related with the total energy dissipation. Therefore, we shall search for an optimal state which maximises the functional $J\{\theta,\boldsymbol{u},p^*,\theta^*\}$ given by

$$\begin{aligned} J = {} & \frac{1}{2}\epsilon\frac{c_p\kappa}{T_0}\Big\langle|\nabla\theta|^2\Big\rangle_{xyz} - \frac{1}{2}\nu\Big\langle|\nabla\boldsymbol{u}|^2\Big\rangle_{xyz} \\ & + \frac{1}{\rho}\left\langle p^*\frac{\partial u_i}{\partial x_i}\right\rangle_{xyz} + \epsilon\frac{c_p}{T_0}\left\langle\theta^*\left(u_j\frac{\partial\theta}{\partial x_j} + v\frac{T_0}{h} - \kappa\frac{\partial^2\theta}{\partial x_j^2}\right)\right\rangle_{xyz}, \end{aligned} \tag{2.19}$$

where ϵ (>0) is the dimensionless weight of the contribution from the heat transfer against the momentum transfer, c_p is specific heat at constant pressure, and $p^*(x,y,z)$ and $\theta^*(x,y,z)$ represent Lagrangian multipliers. We suppose that θ^* satisfies boundary conditions on the walls,

$$\theta^*(y=\pm1) = 0. \tag{2.20}$$

By introducing the following dimensionless quantities

$$x_i' = \frac{x_i}{h}, \quad J' = \frac{J}{U^3/h}, \quad \theta' = \frac{\theta}{T_0}, \quad u_i' = \frac{u_i}{U}, \quad p^{*\prime} = \frac{p^*}{\rho U^2}, \quad \theta^{*\prime} = \frac{\theta^*}{T_0}, \tag{2.21}$$

we rewrite the objective functional (2.19) in a dimensionless form as

$$J = \frac{1}{2}\lambda \frac{1}{RePr}\left\langle |\nabla\theta|^2 \right\rangle_{xyz} - \frac{1}{2}\frac{1}{Re}\left\langle |\nabla \boldsymbol{u}|^2 \right\rangle_{xyz} + \left\langle p^* \frac{\partial u_j}{\partial x_j} \right\rangle_{xyz} + \lambda \left\langle \theta^* \left(u_j \frac{\partial \theta}{\partial x_j} + v - \frac{1}{RePr}\frac{\partial^2 \theta}{\partial x_j^2} \right) \right\rangle_{xyz}, \tag{2.22}$$

where we have dropped the primes attached to the dimensionless quantities,

$$\lambda = \frac{\epsilon}{Ec} \tag{2.23}$$

is new dimensionless weight, and

$$Re = \frac{Uh}{\nu}, \quad Pr = \frac{\nu}{\kappa}, \quad Ec = \frac{U^2}{c_p T_0} \tag{2.24}$$

are the Reynolds number, the Prandtl number, and the Eckert number, respectively. Usually $Ec \ll 1$, and thus we suppose that $\epsilon \ll 1$ so that we may take $\lambda \sim 10^0$. We decompose $\boldsymbol{u}, \theta, p^*$ and θ^* into references and infinitesimal perturbations as

$$\theta = \overline{\theta} + \delta\theta, \quad \boldsymbol{u} = \overline{\boldsymbol{u}} + \delta\boldsymbol{u}, \quad p^* = \overline{p^*} + \delta p^*, \quad \theta^* = \overline{\theta^*} + \delta\theta^*. \tag{2.25}$$

Substituting (2.25) into (2.22), using integration by parts and recalling boundary conditions (2.3), (2.10) and (2.20), we obtain the first variation of J as

$$\begin{aligned} \delta J = &\left\langle \left(-\frac{\partial \overline{p^*}}{\partial x_i} + \frac{1}{Re}\frac{\partial^2 \overline{u_i}}{\partial x_j^2} + \lambda \overline{\theta^*}\frac{\partial \overline{\theta}}{\partial x_i} + \lambda \overline{\theta^*}\delta_{i2} \right) \delta u_i \right\rangle_{xyz} \\ &- \left\langle \lambda \left(\overline{u_j}\frac{\partial \overline{\theta^*}}{\partial x_j} + \frac{1}{RePr}\frac{\partial^2 \overline{\theta^*}}{\partial x_j^2} + \frac{1}{RePr}\frac{\partial^2 \overline{\theta}}{\partial x_j^2} \right) \delta\theta \right\rangle_{xyz} \\ &+ \left\langle \lambda \left(\overline{u_j}\frac{\partial \overline{\theta}}{\partial x_j} + \overline{v} - \frac{1}{RePr}\frac{\partial^2 \overline{\theta}}{\partial x_j^2} \right) \delta\theta^* \right\rangle_{xyz} \\ &+ \left\langle \left(\frac{\partial \overline{u_i}}{\partial x_i} \right) \delta p^* \right\rangle_{xyz}. \end{aligned} \tag{2.26}$$

A stationary point, at which the first variation of J vanishes, i.e. $\delta J = 0$, for any perturbation $\delta\boldsymbol{u}, \delta\theta, \delta\theta^*$ and δp^*, is determined by the Euler–Lagrange equations

$$\frac{\delta J}{\delta u_i} \equiv -\frac{\partial p^*}{\partial x_i} + \frac{1}{Re}\frac{\partial^2 u_i}{\partial x_j^2} + \lambda\theta^*\frac{\partial \theta}{\partial x_i} + \lambda\theta^*\delta_{i2} = 0, \tag{2.27}$$

$$\frac{\delta J}{\delta \theta} \equiv u_j \frac{\partial \theta^*}{\partial x_j} + \frac{1}{RePr}\frac{\partial^2 \theta^*}{\partial x_j^2} + \frac{1}{RePr}\frac{\partial^2 \theta}{\partial x_j^2} = 0, \tag{2.28}$$

$$\frac{\delta J}{\delta \theta^*} \equiv u_j \frac{\partial \theta}{\partial x_j} + v - \frac{1}{RePr}\frac{\partial^2 \theta}{\partial x_j^2} = 0, \tag{2.29}$$

$$\frac{\delta J}{\delta p^*} \equiv \frac{\partial u_i}{\partial x_i} = 0. \tag{2.30}$$

3. Numerical procedures

3.1. *Finding initial guesses*

We find velocity fields which give a maximal value of the objective functional J with a combination of the steepest ascent method and the Newton–Krylov method. To globally seek a maximal point of J, we start with finding initial guesses in the following procedure.

Step. 1 Start from an arbitrary velocity field $\boldsymbol{u}$ which satisfies the continuity equation (2.1) and boundary condition (2.3).

Step. 2 For given $\boldsymbol{u}$, solve equation (2.29) to obtain θ.

Step. 3 For given $\boldsymbol{u}$ and obtained θ from Step. 2, solve equation (2.28) to find θ^*.

Step. 4 Since $\boldsymbol{u}$, θ, and θ^* respectively satisfy the Euler–Lagrange equations (2.28)–(2.30), the first variation δJ can be expressed, in terms of the only functional derivative $\widehat{u}_i \equiv \delta J/\delta u_i$, as

$$\delta J = \langle \widehat{u}_i \delta u_i \rangle_{xyz}. \tag{3.1}$$

Using the functional derivative $\widehat{\boldsymbol{u}}$, renew the velocity field as

$$\boldsymbol{u}^{\mathrm{new}} = \boldsymbol{u} + s\widehat{\boldsymbol{u}}, \tag{3.2}$$

where s is a small positive constant to be taken as $s \sim 10^{-2}$.

Step. 5 Repeat Step. 2 – Step. 4.

Since (3.2) implies that

$$\frac{\partial u_i^{\mathrm{new}}}{\partial x_i} = \frac{\partial u_i}{\partial x_i} + s\frac{\partial \widehat{u}_i}{\partial x_i} = s\frac{\partial \widehat{u}_i}{\partial x_i}, \tag{3.3}$$

in order that $\boldsymbol{u}^{\mathrm{new}}$ is incompressible we invoke the continuity for $\widehat{\boldsymbol{u}}$,

$$\frac{\partial \widehat{u}_i}{\partial x_i} = 0. \tag{3.4}$$

Taking the double curl, the single curl and the xz-average of equation (2.27), we have the equations for the wall-normal velocity v, the wall-normal vorticity ω_y, and the averaged velocities,

$$\frac{\partial^2 \widehat{v}}{\partial x_j^2} = \frac{1}{Re}\frac{\partial^2}{\partial x_j^2}\frac{\partial^2 v}{\partial x_j^2} + \lambda H_v + \lambda\left(\frac{\partial^2}{\partial x^2} + \frac{\partial^2}{\partial z^2}\right)\theta^*, \tag{3.5}$$

$$\widehat{\omega}_y = \frac{1}{Re}\frac{\partial^2 \omega_y}{\partial x_j^2} + \lambda H_\omega, \tag{3.6}$$

$$\langle \widehat{u} \rangle_{xz} = \frac{1}{Re}\frac{\mathrm{d}^2\langle u \rangle_{xz}}{\mathrm{d}y^2} + \lambda\left\langle \theta^*\frac{\partial \theta}{\partial x}\right\rangle_{xz}, \tag{3.7}$$

$$\langle \widehat{w} \rangle_{xz} = \frac{1}{Re}\frac{\mathrm{d}^2\langle w \rangle_{xz}}{\mathrm{d}y^2} + \lambda\left\langle \theta^*\frac{\partial \theta}{\partial z}\right\rangle_{xz} \tag{3.8}$$

with

$$H_v = -\frac{\partial}{\partial y}\left[\frac{\partial}{\partial x}\left(\theta^*\frac{\partial \theta}{\partial x}\right) + \frac{\partial}{\partial z}\left(\theta^*\frac{\partial \theta}{\partial z}\right)\right] + \left(\frac{\partial^2}{\partial x^2} + \frac{\partial^2}{\partial z^2}\right)\left(\theta^*\frac{\partial \theta}{\partial y}\right), \tag{3.9}$$

$$H_\omega = \frac{\partial}{\partial z}\left(\theta^*\frac{\partial \theta}{\partial x}\right) - \frac{\partial}{\partial x}\left(\theta^*\frac{\partial \theta}{\partial z}\right), \tag{3.10}$$

from which p^* has been eliminated. The corresponding boundary conditions are

$$v(y=\pm1)=\frac{\partial v}{\partial y}(y=\pm1)=0, \tag{3.11a}$$

$$\omega_y(y=\pm1)=0, \tag{3.11b}$$

$$\langle u\rangle_{xz}(y=\pm1)=\pm1, \tag{3.11c}$$

$$\langle w\rangle_{xz}(y=\pm1)=0, \tag{3.11d}$$

$$\theta(y=\pm1)=0, \tag{3.11e}$$

$$\theta^*(y=\pm1)=0. \tag{3.11f}$$

In the periodic streamwise and spanwise directions, $\boldsymbol{u}$, vorticity $\boldsymbol{\omega}=\nabla\times\boldsymbol{u}$, θ, and θ^* are approximated by truncated Fourier series

$$(\boldsymbol{u},\boldsymbol{\omega},\theta,\theta^*)=\sum_{k=-K}^{K}\sum_{m=-M}^{M}\left(\widetilde{\boldsymbol{u}}^{km},\widetilde{\boldsymbol{\omega}}^{km},\widetilde{\theta}^{km},\widetilde{\theta^*}^{km}\right)\mathrm{e}^{\mathrm{i}2\pi kx/L_x}\mathrm{e}^{\mathrm{i}2\pi mz/L_z}, \tag{3.12}$$

where K and M are positive integers. Note that the Fourier coefficients of u and w for $(k,m)\neq(0,0)$ are given by $\widetilde{v}^{km}$ and $\widetilde{\omega_y}^{km}$ through

$$\widetilde{u}^{km}=\mathrm{i}\frac{(2\pi k/L_x)\mathrm{d}\widetilde{v}^{km}/\mathrm{d}y+(2\pi m/L_z)\widetilde{\omega_y}^{km}}{4\pi^2(k^2/L_x^2+m^2/L_z^2)}, \tag{3.13}$$

$$\widetilde{w}^{km}=\mathrm{i}\frac{(2\pi m/L_z)\mathrm{d}\widetilde{v}^{km}/\mathrm{d}y+(2\pi k/L_x)\widetilde{\omega_y}^{km}}{4\pi^2(k^2/L_x^2+m^2/L_z^2)}. \tag{3.14}$$

In the wall-normal direction, $\widetilde{v}^{km}$, $\widetilde{\omega_y}^{km}$, $\langle u\rangle_{xz}-y$, $\langle w\rangle_{xz}$, $\widetilde{\theta}^{km}$ and $\widetilde{\theta^*}^{km}$ are expanded, in terms of the polynomials which satisfy boundary conditions (3.11), as

$$\widetilde{v}^{km}=\sum_{n=0}^{N-4}c_v^{kmn}\left(T_n-2\frac{n+2}{n+3}T_{n+2}+\frac{n+1}{n+3}T_{n+4}\right), \tag{3.15a}$$

$$\left(\widetilde{\omega_y}^{km},\widetilde{\theta}^{km},\widetilde{\theta^*}^{km}\right)=\sum_{n=0}^{N-2}\left(c_\omega^{kmn},c_\theta^{kmn},c_{\theta^*}^{kmn}\right)\left(T_n-T_{n+2}\right), \tag{3.15b}$$

$$\begin{aligned}(\langle u\rangle_{xz}-y,\langle w\rangle_{xz})=&\frac{3}{2}\left(\langle u\rangle_{xyz},\langle w\rangle_{xyz}\right)\left(1-y^2\right)\\&+\frac{\mathrm{d}}{\mathrm{d}y}\left\{\sum_{n=0}^{N-4}(c_u^n,c_w^n)\left(T_n-2\frac{n+2}{n+3}T_{n+2}+\frac{n+1}{n+3}T_{n+4}\right)\right\},\end{aligned} \tag{3.15c}$$

where $T_n(y)$ represents the n-th order Chebyshev polynomial. The nonlinear terms are evaluated using a spectral collocation method. Aliasing errors are removed with the aid of the 2/3 rule for the Fourier transform and the 1/2 rule for the Chebyshev transform.

3.2. *Newton–Krylov iteration*

In nonlinear dynamical systems stemming from the Navier–Stokes equation, a combination of the Newton–Raphson method and the Krylov subspace method has been used to efficiently obtain nonlinear equilibrium and periodic solutions (Viswanath 2007, 2009). In this study, employing the initial guesses obtained as mentioned in §3.1, we perform

the Newton–Krylov iteration to find nonlinear solutions to the Euler–Lagrange equations (2.27)–(2.30).

Introducing pseudo-time derivative terms $\partial(\cdot)/\partial\tau$ into equations (3.5)–(3.8), the xyz-average of equation (2.27), equations (2.28) and (2.29), we have the following nonlinear evolution equations

$$\frac{\partial}{\partial\tau}\frac{\partial^2 v}{\partial x_j^2} = \frac{1}{Re}\frac{\partial^2}{\partial x_j^2}\frac{\partial^2 v}{\partial x_j^2} + \lambda H_v + \lambda\left(\frac{\partial^2}{\partial x^2} + \frac{\partial^2}{\partial z^2}\right)\theta^*, \tag{3.16}$$

$$\frac{\partial}{\partial\tau}\omega_y = \frac{1}{Re}\frac{\partial^2\omega_y}{\partial x_j^2} + \lambda H_\omega, \tag{3.17}$$

$$\frac{\partial}{\partial\tau}\langle u\rangle_{xz} = \frac{1}{Re}\frac{\mathrm{d}^2\langle u\rangle_{xz}}{\mathrm{d}y^2} + \lambda\left\langle\theta^*\frac{\partial\theta}{\partial x}\right\rangle_{xz}, \tag{3.18}$$

$$\frac{\partial}{\partial\tau}\langle w\rangle_{xz} = \frac{1}{Re}\frac{\mathrm{d}^2\langle w\rangle_{xz}}{\mathrm{d}y^2} + \lambda\left\langle\theta^*\frac{\partial\theta}{\partial z}\right\rangle_{xz}, \tag{3.19}$$

$$\frac{\partial}{\partial\tau}\langle u\rangle_{xyz} = \frac{1}{2Re}\left[\frac{\mathrm{d}\langle u\rangle_{xz}}{\mathrm{d}y}\right]_{y=-1}^{y=+1} + \lambda\left\langle\theta^*\frac{\partial\theta}{\partial x}\right\rangle_{xyz}, \tag{3.20}$$

$$\frac{\partial}{\partial\tau}\langle w\rangle_{xyz} = \frac{1}{2Re}\left[\frac{\mathrm{d}\langle w\rangle_{xz}}{\mathrm{d}y}\right]_{y=-1}^{y=+1} + \lambda\left\langle\theta^*\frac{\partial\theta}{\partial z}\right\rangle_{xyz}, \tag{3.21}$$

$$\frac{\partial}{\partial\tau}\theta^* = u_j\frac{\partial\theta^*}{\partial x_j} + \frac{1}{RePr}\frac{\partial^2\theta^*}{\partial x_j^2} + \frac{1}{RePr}\frac{\partial^2\theta}{\partial x_j^2}, \tag{3.22}$$

$$\frac{\partial}{\partial\tau}\theta = u_j\frac{\partial\theta}{\partial x_j} + v - \frac{1}{RePr}\frac{\partial^2\theta}{\partial x_j^2}, \tag{3.23}$$

'steady' solutions to which satisfy the Euler–Lagrange equations (2.27)–(2.30). By using a spectral Galerkin method, we can convert equations (3.16)–(3.23) into a nonlinear autonomous dynamical system

$$\frac{\mathrm{d}\boldsymbol{X}}{\mathrm{d}\tau} = \boldsymbol{F}(\boldsymbol{X}; Re, Pr, \lambda), \tag{3.24}$$

where $\boldsymbol{X}(\tau)$ represents a state point in the phase space spanned by the Fourier–Chebyshev coefficients of $v, \omega_y, \langle u\rangle_{xz}, \langle w\rangle_{xz}, \theta$ and θ^*. The time advancement is carried out by the Crank–Nicholson scheme for the diffusion terms and the 2nd-order Adams–Bashforth scheme for the others.

Let $\overline{\boldsymbol{X}}$ be an initial guess to find a maximal point of J. Integrating equation (3.24), we define the flow map as

$$\boldsymbol{X} = \boldsymbol{G}(\overline{\boldsymbol{X}}, \tau) \tag{3.25}$$

for any 'time' τ, where $\boldsymbol{G}(\overline{\boldsymbol{X}}, 0) = \overline{\boldsymbol{X}}$. Supposing that $\overline{\boldsymbol{X}}$ is sufficiently close to a stationary point and thus $\delta\boldsymbol{X}$ is a small correction vector, we linearise equation (3.25) at $\boldsymbol{X} = \overline{\boldsymbol{X}}$ to obtain

$$\boldsymbol{A}\delta\boldsymbol{X} = \boldsymbol{B}, \tag{3.26}$$

where

$$\boldsymbol{A} = \frac{\partial\boldsymbol{G}}{\partial\boldsymbol{X}}(\overline{\boldsymbol{X}}) - \boldsymbol{I}, \qquad \boldsymbol{B} = \overline{\boldsymbol{X}} - \boldsymbol{G}(\overline{\boldsymbol{X}}), \tag{3.27}$$

$\boldsymbol{I}$ being an identity matrix with the same dimension as the Jacobian matrix $\partial\boldsymbol{G}/\partial\boldsymbol{X}$. By

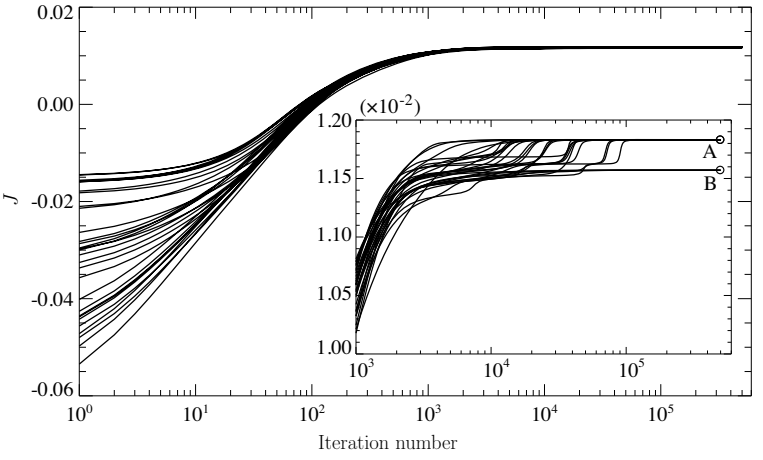

FIGURE 2. Objective functional J against the number of the iteration described in § 3.1 for various initial guesses at $Re = 100$ for $Pr = 1$ and $\lambda = 1$. 30 initial guesses (10 each) are taken from turbulent flow fields at $Re = 1000$, $Re = 2000$ and $Re = 3000$. 26 of them converge to a local maximum A, and the others tend to a local maximum B.

solving the linear equation (3.26) the correction vector $\delta\boldsymbol{X}$ is obtained to renew $\overline{\boldsymbol{X}}$ as

$$\overline{\boldsymbol{X}}^{\mathrm{new}} = \overline{\boldsymbol{X}} + \delta\boldsymbol{X}. \tag{3.28}$$

We iterate the procedure until a termination criterion

$$\frac{||\boldsymbol{G}(\overline{\boldsymbol{X}}) - \overline{\boldsymbol{X}}||_2}{||\overline{\boldsymbol{X}}||_2} < 10^{-12} \tag{3.29}$$

is satisfied, where $||\cdot||_2$ denotes an L^2-norm. To solve equation (3.26) we use the GMRES method (Saad & Schultz 1986) which is one of the Krylov subspace methods. In this method, an approximation of a correction vector $\delta\boldsymbol{X}$ can be got without calculating matrix A, by minimising the norm of a residual vector in a Krylov subspace.

3.3. *Direct numerical simulation of turbulent plane Couette flow*

For comparison with optimal states obtained by the maximisation of the functional J, direct numerical simulations are also performed for turbulent momentum and heat transfer in plane Couette flow. In the simulations we numerically integrate the incompressible Navier–Stokes equation and the advection-diffusion equation for a passive scalar, i.e. temperature, supplemented by boundary conditions (2.3). The evolution equations are discretised employing a spectral Galerkin method based on the expansions (3.12) and (3.15). Time marching of the equations is done with a combination of the Crank–Nicholson and 2nd-order Adams–Bashforth scheme. The Prandtl number Pr is set to unity. Turbulence data are accumulated in the range of the Reynolds number, $Re = 500$–10000, in a computational domain of $(L_x, L_y, L_z) = (2\pi, 2, \pi)$.

3.4. *Global convergence and dependence on domain size*

We perform the maximisation of the functional J starting with 30 different initial guesses extracted from turbulent flow fields in order to examine the dependence of a computed local maximum on the initial guesses. Figure 2 shows the functional J against the number of the iteration mentioned in § 3.1 for the distinct 30 initial guesses at $Re = 100$ for $Pr = 1$ and $\lambda = 1$. For all the initial guesses, the value of J rapidly

Label	J	ε_S	ε_E
A	1.18×10^{-2}	5.17×10^{-2}	2.81×10^{-2}
B	1.16×10^{-2}	5.27×10^{-2}	2.96×10^{-2}

TABLE 1. Two local maxima of objective functional J at $Re = 100$ for $Pr = 1$ and $\lambda = 1$.

Re	Pr	λ	L_x	L_z	(N_x, N_y, N_z)	J	ε_S	ε_E
1000	1.0	0.1	π	π	(32,128,256)	0.65×10^{-5}	1.70×10^{-2}	1.69×10^{-3}
1000	1.0	0.1	2π	π	(32,128,256)	4.42×10^{-5}	1.62×10^{-2}	1.53×10^{-3}
1000	1.0	0.1	3π	π	(64,128,256)	3.97×10^{-5}	1.58×10^{-2}	1.50×10^{-3}
1000	1.0	0.1	2π	0.5π	(32,128,256)	3.39×10^{-5}	1.63×10^{-2}	1.56×10^{-3}
1000	1.0	0.1	2π	1.5π	(64,128,256)	2.65×10^{-5}	1.60×10^{-2}	1.55×10^{-3}
1000	1.0	0.1	2π	2π	(64,128,512)	1.24×10^{-5}	1.60×10^{-2}	1.58×10^{-3}

TABLE 2. Dependence on computational domain size

approaches the vicinity of the two local maxima to be mentioned just below. We have eventually obtained the two different local maxima (the larger local maximum is labeled as A, and the smaller one as B). Table 1 compares the values of J together with the total scalar dissipation ε_S and the total energy dissipation ε_E,

$$\varepsilon_S = \frac{1}{RePr}\left\langle |\nabla T|^2 \right\rangle_{xyz}, \quad \varepsilon_E = \frac{1}{Re}\left\langle |\nabla \boldsymbol{u}|^2 \right\rangle_{xyz}, \tag{3.30}$$

between the local maxima A and B. The present objective functional J has multimodality, but there appear only two local maxima for many initial guesses.

The optimal velocity fields exhibit three-dimensional structures which consist of large-scale streamwise circulation rolls and smaller-scale quasi-streamwise vortex tubes near the wall (see figures 5 and 6). The size of the large rolls corresponds to half the spanwise period $L_z/2$. Table 2 summarises each maximal state obtained in the various domains at $Re = 1000$ for $Pr = 1$ and $\lambda = 0.1$. It is found that J takes the largest value for $(L_x, L_z) = (2\pi, \pi)$ among $(L_x, L_z) = (\pi, \pi)$, $(2\pi, \pi)$, $(3\pi, \pi)$; $(2\pi, 0.5\pi)$, $(2\pi, \pi)$, $(2\pi, 1.5\pi)$, $(2\pi, 2\pi)$, suggesting that there exist finite values of the streamwise and spanwise periods which lead to the global optimal. However, our goal in this paper is not to identify the optimal domain for all the parameters including Re. As will be described below, the velocity fields, which are realised as a solution to the Euler–Lagrange equations (2.27)-(2.30), have extremely high performance for heat transfer and exhibit qualitatively similar flow structures being roughly independent of (L_x, L_z). In the following, therefore, we shall choose the domain size $(L_x, L_y, L_z) = (2\pi, 2, \pi)$ to discuss characteristic flow structures and the mechanism of heat transfer enhancement. The effects of the domain size on the scalar dissipation and the energy dissipation can be seen to be minor.

3.5. *Effects of weight λ on optimal state*

We next consider the effects on the optimal state of the weight λ of the scalar dissipation in the objective functional J.

Let us first note that in the special case of a streamwise-independent two-dimensional velocity field the weight λ can be removed from the Euler–Lagrange equations (2.27)–

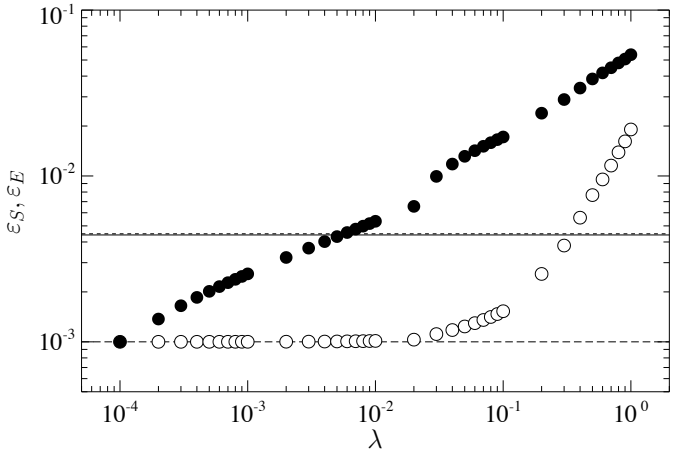

FIGURE 3. Total scalar and energy dissipation as a function of the weight λ for the optimal state at $Re = 1000$ for $Pr = 1$: •, the total scalar dissipation ε_S; ∘, the energy dissipation ε_E. The long-dashed line indicates ε_S or ε_E in a laminar state, $1/Re = 10^{-3}$. The solid and short-dashed line respectively represent the time-averaged ε_S and ε_E in turbulent flow at $Re = 1000$ for $Pr = 1$.

(2.30) as follows. Taking the curl of equation (2.27), we have

$$\frac{1}{\lambda Re}\frac{\partial^2 \omega_x}{\partial x_j^2} + \frac{\partial(\theta^*, \theta)}{\partial(y, z)} + \frac{\partial \theta^*}{\partial z} = 0, \tag{3.31}$$

where

$$\frac{\partial(\beta, \gamma)}{\partial(y, z)} = \frac{\partial \beta}{\partial y}\frac{\partial \gamma}{\partial z} - \frac{\partial \beta}{\partial z}\frac{\partial \gamma}{\partial y} \tag{3.32}$$

is the Jacobian determinant. The streamwise-independent velocity field can be expressed, in terms of the streamfunction $\psi(y, z)$, as

$$(u, v, w) = \left(y, \frac{\partial \psi}{\partial z}, -\frac{\partial \psi}{\partial y}\right), \tag{3.33}$$

where the streamwise velocity u has been uniquely determined from the x-component of equation (2.27) and its independence of the x-direction ($\partial u/\partial x = 0$). The streamfunction is related to the streamwise vorticity via the Poisson equation

$$\frac{\partial^2 \psi}{\partial x_j^2} = -\omega_x. \tag{3.34}$$

Using ψ, equations (2.28) and (2.29) are respectively rewritten as

$$RePr\left[-\frac{\partial(\psi, \theta^*)}{\partial(y, z)}\right] + \frac{\partial^2}{\partial x_j^2}(\theta^* + \theta) = 0, \tag{3.35}$$

$$RePr\left[-\frac{\partial(\psi, \theta)}{\partial(y, z)} + \frac{\partial \psi}{\partial z}\right] - \frac{\partial^2 \theta}{\partial x_j^2} = 0. \tag{3.36}$$

The boundary conditions of ψ are

$$\psi(y = \pm 1) = \frac{\partial \psi}{\partial y}(y = \pm 1) = 0. \tag{3.37}$$

Introducing the new variable and the new parameter as

$$\psi^* = \frac{\psi}{\sqrt{\lambda}}, \quad Re^* = \sqrt{\lambda} Re \tag{3.38}$$

and using equation (3.34), the Euler–Lagrange equations can be rewritten in the streamwise-independent case as

$$-\frac{1}{Re^*}\frac{\partial^2}{\partial x_j^2}\frac{\partial^2 \psi^*}{\partial x_j^2} + \frac{\partial(\theta^*, \theta)}{\partial(y, z)} + \frac{\partial \theta^*}{\partial z} = 0, \tag{3.39}$$

$$Re^* Pr \left[-\frac{\partial(\psi^*, \theta^*)}{\partial(y, z)} \right] + \frac{\partial^2}{\partial x_j^2}(\theta^* + \theta) = 0, \tag{3.40}$$

$$Re^* Pr \left[-\frac{\partial(\psi^*, \theta)}{\partial(y, z)} + \frac{\partial \psi^*}{\partial z} \right] - \frac{\partial^2 \theta}{\partial x_j^2} = 0, \tag{3.41}$$

which are supplemented by the boundary conditions of ψ^*,

$$\frac{\partial \psi^*}{\partial z}(y = \pm 1) = \frac{\partial \psi^*}{\partial y}(y = \pm 1) = 0. \tag{3.42}$$

Figure 3 shows the total scalar dissipation ε_S and the energy dissipation ε_E as a function of λ for the optimal state at $Re = 1000$, which will turn out to be three-dimensional for $\lambda = 0.1$ in § 4.1. Note that in the case of $\lambda = 0$, a laminar state indicated by the long-dashed line is optimal since laminar flow gives lower bound for the energy dissipation of an arbitrary velocity field, that is,

$$\varepsilon_E = \frac{1}{Re} \left\langle |\nabla \boldsymbol{u}|^2 \right\rangle_{xyz} \geqslant \frac{1}{Re}. \tag{3.43}$$

The weight λ is a factor to control the contribution of the scalar dissipation against the energy dissipation in the optimisation of J. Decreasing λ means that the weight of the energy dissipation is increased relative to the scalar dissipation. As a result, an optimal state has the smaller energy dissipation (in other words, the smaller enstrophy). For large λ, the significantly high scalar dissipation (i.e., high heat flux) is achieved with the larger energy dissipation. In light of heat transfer enhancement, we should find an optimal state with a higher heat flux and smaller energy dissipation than uncontrolled turbulent flow. In plane Couette flow at $Re = 1000$, a sustained turbulent state can be observed. In figure 3, the solid and short-dashed line respectively represent the time-averaged scalar and energy dissipation of turbulent flow at $Re = 1000$ for $Pr = 1$. Their consistency is attributed to the similarity between turbulent heat and momentum transfer. In the range of $0.02 < \lambda < 0.4$, we can find the optimal states of higher heat transfer and lower energy dissipation than the turbulent state. In this range of the weight λ we have confirmed that the optimised velocity fields do not exhibit significantly different flow structures depending on λ.

In the following sections we shall present the optimal states in the domain $(L_x, L_y, L_z) = (2\pi, 2, \pi)$ for $Pr = 1$ and $\lambda = 0.1$. The numerical solutions have been obtained on grid points $(N_x, N_y, N_z) = (32, 128, 256)$ at $Re = 30 - 900$ and $(N_x, N_y, N_z) = (32, 256, 512)$ at $Re = 1000 - 10000$.

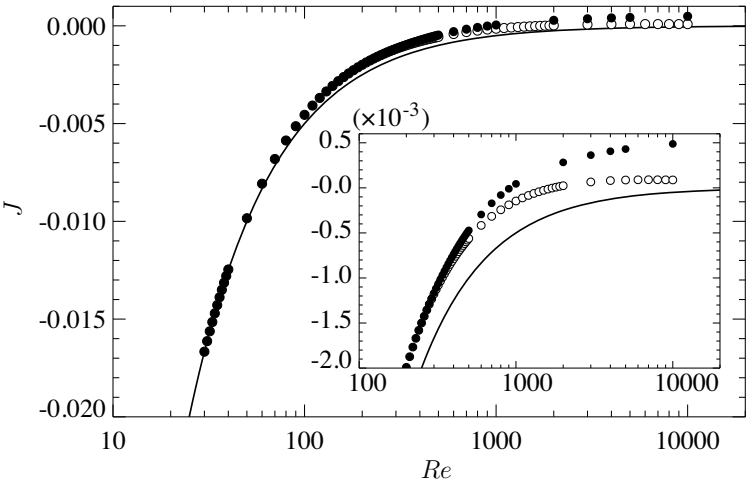

FIGURE 4. The maximal value of J as a function of Re for $\lambda = 0.1$. Filled circles represent the value of J for the optimal states, and open circles denote maximised J only within a streamwise-independent two-dimensional velocity field. The solid curve represents the value of J for the laminar solution, $J = -1/(2Re)$.

4. Characteristics of optimal states

4.1. *Flow and temperature field*

Figure 4 shows the maximal value of J as a function of Re for $\lambda = 0.1$. The maximised J only within a streamwise-independent two-dimensional velocity field is also plotted for comparison purposes. The solid curve represents the value of J for the laminar solution $\boldsymbol{u} = y\mathbf{e}_x$, which is the lower bound of J. At low values of Re, the optimal state exhibits a streamwise-independent two-dimensional velocity field as seen in figure 5, where the isosurfaces of the positive and negative streamwise vorticity ω_x are shown for the optimal states at $Re = 50$, 200, 1000 and 5000. At the higher Reynolds numbers Re= 1000, 5000, streamwise-dependent three-dimensional structures, i.e. spanwise-inclined vortex tubes, with stronger ω_x appear near the wall. We shall discuss the onset of the spanwise inclination of the structures and its effects on heat transfer in § 6. In figure 5(*c,d*), only the isosurfaces in the lower half of the channel ($y < 0$) are shown for visualization of the near-wall vortices. At Re= 5000 a large number of smaller vortex structures with much stronger ω_x are observed in the close vicinity of the wall. Note that such small-scale intense vortices do not emerge near the wall in the two-dimensional optimal velocity fields (figure 5*a,b*). Although the formation of the small-scale structures increases the energy dissipation, it also significantly enhances the scalar dissipation. As a result of these counteractions, the three-dimensional fields could be an optimal state at higher Re. Even when the domain size or the weight λ is changed, we have obtained the optimal states which represent qualitatively similar three-dimensional structures.

Figure 6(*a-d*) shows the cross-stream velocity field (w, v) and the temperature field T in the optimal states at $Re = 50$, 200, 1000 and 5000. The two-dimensional optimal states at $Re = 50, 200$ (figure 6*a,b*) consist of the two large-scale circulation rolls which are reminiscent of thermal convection and play a role in heat transfer from the upper wall to the lower wall. Near the walls, the regions with the high temperature gradient are formed by the effects of the circulation rolls, and the gradient gets higher as Re increases. Meanwhile, the three-dimensional optimal state at $Re = 1000, 5000$ (figure 6*c,d*) exhibit the more complicated flow and temperature field. Similar to the two-dimensional states,

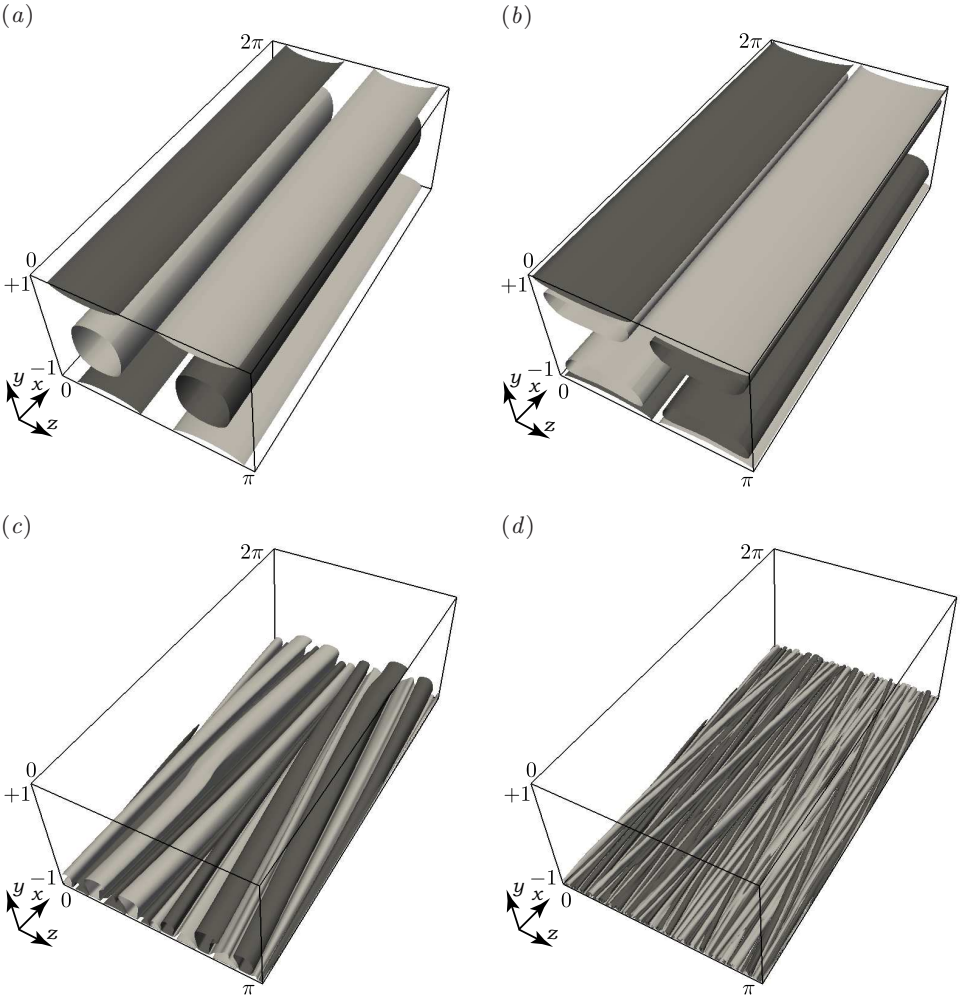

FIGURE 5. Isosurfaces of the streamwise vorticity in the optimal states at (*a*) $Re = 50$, (*b*) $Re = 200$, (*c*) $Re = 1000$ and (*d*) $Re = 5000$, for $\lambda = 0.1$. In (*c*) and (*d*), only the isosurfaces in the lower half of the channel ($y < 0$) are shown for visualization of the small-scale vortex structures near the lower wall. Light (or dark) grey objects represent isosurfaces of (*a*) $\omega_x = +0.25$ (or -0.25), (*b*) $\omega_x = +0.25$ (or -0.25), (*c*) $\omega_x = +0.5$ (or -0.5), (*d*) $\omega_x = +2$ (or -2).

there are the large-scale circulation rolls with the width of half the spanwise period L_z ($= \pi$). The wall-normal component of the velocity is dominant in between the circulation rolls. Small-scale vortices are observed only in the near-wall regions. They produce the regions with high temperature gradient by pushing the hotter (or colder) fluid onto the lower (or upper) wall. In figure 6(*e,f*) are shown the streamwise-averaged cross-stream velocity fields at $Re = 1000$ and 5000. Even in the averaged fields, the effects of the small-scale vortices can be seen close to the wall at $Re = 5000$.

The mean temperature and the mean streamwise velocity profiles of the optimal states are shown in figure 7(*a*). As Re increases, the mean temperature profile is more flattened in the central region of the channel, while the temperature gradient at the walls is higher. On the other hand, the mean velocity profile is almost consistent with a laminar profile. For the streamwise-independent case (i.e., $\partial(\cdot)/\partial x = 0$) seen in the optimal state at $Re =$

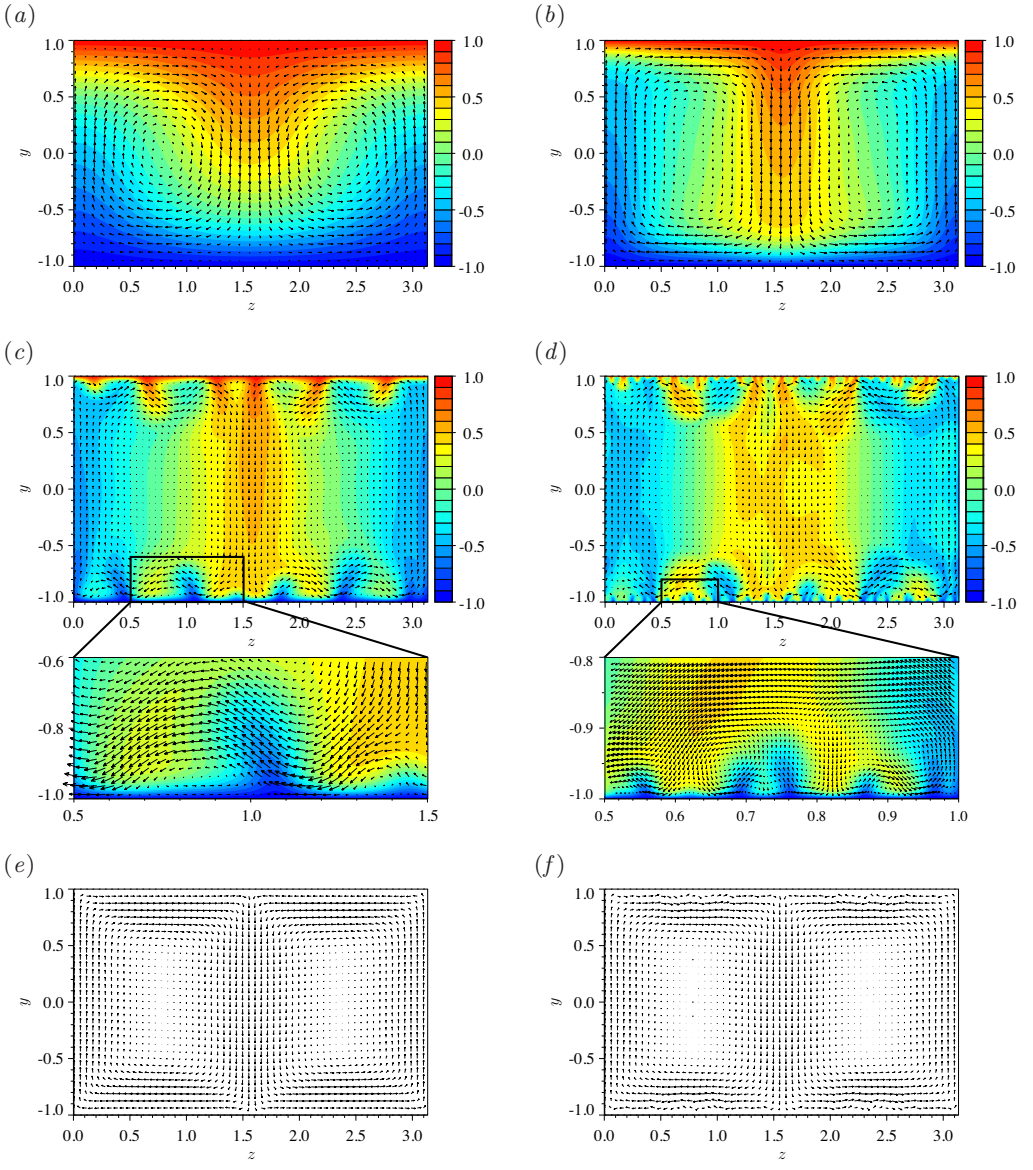

FIGURE 6. (Colour online) Velocity and temperature fields in the optimal state at (a) $Re = 50$, (b) $Re = 200$, (c,e) $Re = 1000$ and (d,f) $Re = 5000$, for $\lambda = 0.1$. (a,b,c,d) The cross-stream velocity vectors (w, v) and contours of the temperature field T in the plane $x = 0$. In (c) and (d), the enlarged views of the near-wall region are also shown. (e,f) The streamwise-averaged cross-stream velocity vectors $(\langle w \rangle_x, \langle v \rangle_x)$.

200, the streamwise velocity u is strictly consistent with the laminar profile $u = y$, which is a consequence of the x-component of the Euler–Lagrange equation (2.27). At large Re, the three-dimensional vortex structure has appeared to bring about the deviation from the laminar profile, shown in figure 7(b), although the deviation is small even at $Re = 5000$.

4.2. *Wall heat flux and energy dissipation*

Let us now consider the Stanton number St and the friction coefficient C_f which are

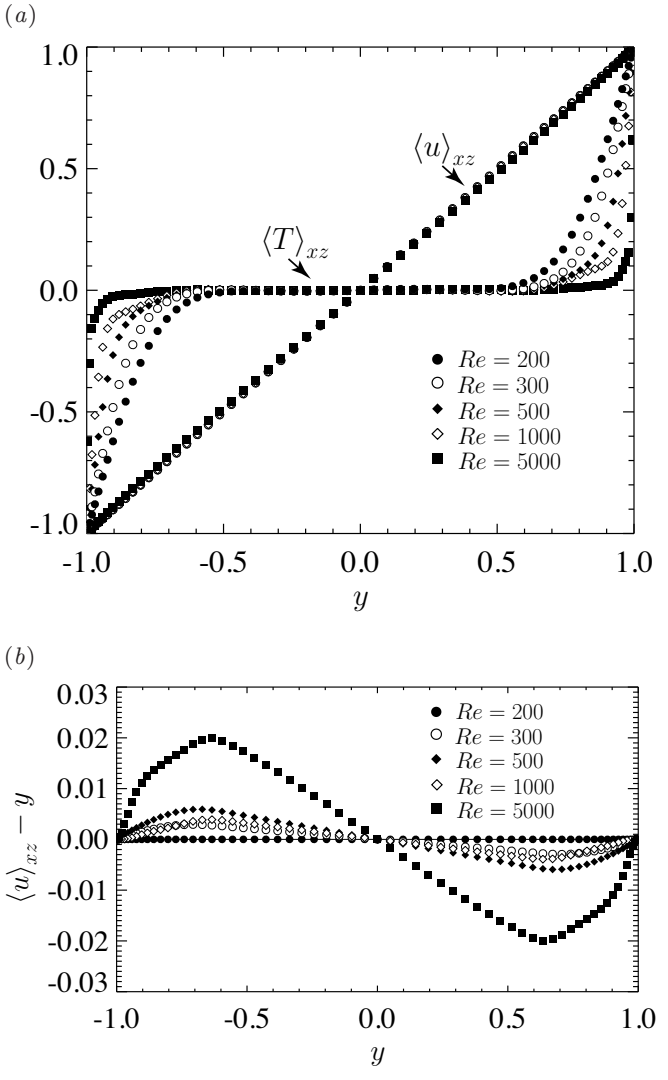

FIGURE 7. Mean temperature and velocity profiles in the optimal state for $\lambda = 0.1$. (a) The mean temperature $\langle T \rangle_{xz}$ and the mean streamwise velocity $\langle u \rangle_{xz}$. (b) The deviation of the mean streamwise velocity from the laminar flow, $\langle u \rangle_{xz} - y$.

respectively defined as

$$St = \frac{1}{RePr}\left[\frac{\mathrm{d}}{\mathrm{d}y}\langle T\rangle_{xz}\,(y=+1) + \frac{\mathrm{d}}{\mathrm{d}y}\langle T\rangle_{xz}\,(y=-1)\right], \tag{4.1}$$

$$C_f = \frac{1}{Re}\left[\frac{\mathrm{d}}{\mathrm{d}y}\langle u\rangle_{xz}(y=+1) + \frac{\mathrm{d}}{\mathrm{d}y}\langle u\rangle_{xz}(y=-1)\right]. \tag{4.2}$$

Note that the similarity between heat and momentum transfer implies that $St \approx C_f$ for $Pr = 1$. Figure 8(a) shows St and C_f in the optimal state for $\lambda = 0.1$. The solid line and the dashed curve represent the theoretical formula for laminar flow and the empirical formula (Robertson & Johnson 1970) for turbulent flow, respectively. The time-averaged St and C_f in turbulent flow are also plotted as a reference. In turbulent flow, St and C_f are almost the same due to the similarity between momentum and heat transfer. In

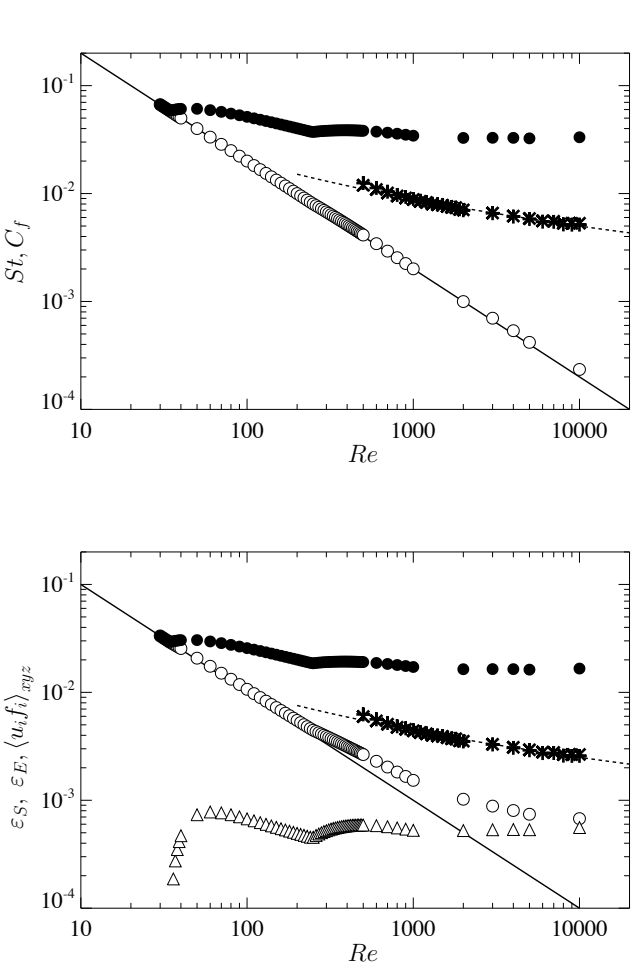

FIGURE 8. (a) Stanton number St and friction coefficient C_f as a function of Re. The optimal state for $\lambda = 0.1$: ●, St; ○, C_f. The turbulent flow: ×, St; +, C_f. The solid line and dashed curve represent $C_f = 2/Re$ for the laminar flow and the empirical formula $C_f = 2(0.2/\log(Re))^2$ for the turbulent flow, respectively. (b) Total scalar dissipation ε_S, energy dissipation ε_E and energy input $\langle u_i f_i \rangle_{xyz}$. The optimal state for $\lambda = 0.1$: ●, ε_S; ○, ε_E; △, $\langle u_i f_i \rangle_{xyz}$. The turbulent flow: ×, ε_S; +, ε_E. The solid line and dashed curve represent $1/Re$ and $C_f/2$ for the laminar flow and the turbulent flow, respectively.

contrast, in the optimal state extremely high St is achieved in comparison with turbulence whilst C_f is comparably low to the laminar flow, decreasing as Re^{-1} with increasing Re.

The dimensionless versions of budget equations (2.15) and (2.18) are given respectively by

$$\varepsilon_S = \frac{1}{2} St, \tag{4.3}$$

$$\varepsilon_E = \frac{1}{2} C_f + \langle u_i f_i \rangle_{xyz}. \tag{4.4}$$

The optimal states found in this work require the external force f_i to satisfy the Navier–Stokes equation, since we have imposed only the divergence-free condition on the velocity field. The external force leads to the additional energy input $\langle u_i f_i \rangle_{xyz}$ which has appeared

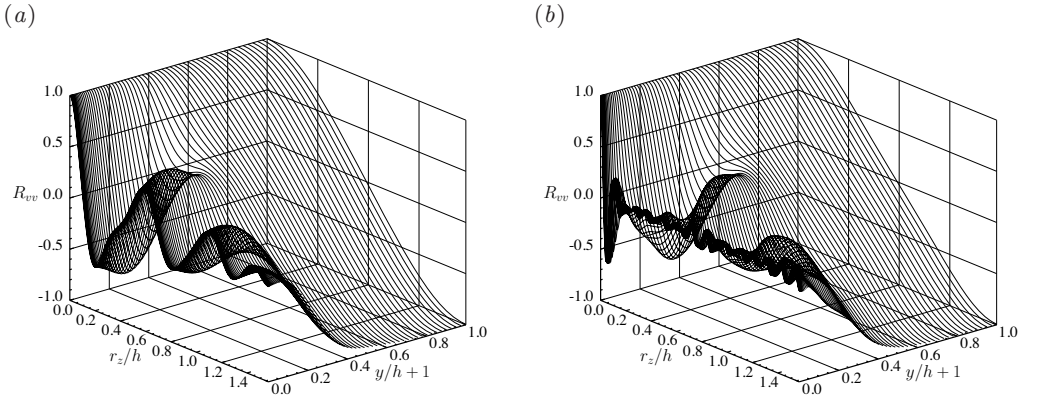

FIGURE 9. Two-point spanwise correlation of the wall-normal velocity R_{vv} for $\lambda = 0.1$. (a) $Re = 1000$, (b) $Re = 5000$.

in equation (4.4). Figure 8(b) shows the total scalar dissipation ε_S, the energy dissipation ε_E and the energy input $\langle u_i f_i \rangle_{xyz}$. Note that in the case of no external force, the energy budget implies $\varepsilon_E = C_f/2$. The solid line represents the energy dissipation in the laminar flow, and provides the lower bound of ε_E. As Re increases, ε_E for the optimal state gradually deviates from that of the laminar flow, because of the relatively greater contribution of the energy input $\langle u_i f_i \rangle_{xyz}$. The energy input is positive (or zero for a laminar solution) at any Re, but it is quite small in comparison to ε_E in the turbulent flow. The significant heat transfer enhancement with small energy dissipation can be confirmed for the optimal state (e.g. $\varepsilon_S/\varepsilon_E \approx 24.6$ at $Re = 10000$). The spatial distribution of the external force and the local energy input are depicted in Appendix A.

5. Hierarchical structure in optimal state

Let us discuss the hierarchical structure and its scaling for the optimal state. Just in this section, we restore the dimensional variables, such as $\boldsymbol{x}, \boldsymbol{u}, T$. As mentioned in §4.1, a number of quasi-streamwise vortex tubes appear near the walls at large Re. In order to quantitatively evaluate their size at each distance to the wall, we introduce a two-point spanwise correlation function of the wall-normal velocity defined by

$$R_{vv}(r_z; y) = \frac{\langle v(x, y, z) v(x, y, z + r_z) \rangle_{xz}}{\langle v(x, y, z)^2 \rangle_{xz}}, \tag{5.1}$$

where r_z indicates the spacing between two points separated in the z-direction. The correlation R_{vv} is shown for the optimal states at $Re = 1000$ and 5000 in figure 9, where r_z and the distance from the lower wall, $y + h$, are normalized by the channel half height h. At the midplane of the channel, $y/h+1 = 1$, R_{vv} has only one local minimum, since the wall-normal velocity component is predominantly induced by the large-scale circulation rolls in the central region of the channel. At the smaller values of $y/h + 1$, i.e. the closer positions to the wall, however, oscillatory behaviour can be seen in R_{vv}. The wavelength of the oscillation corresponds to the size of the spanwise-arranged quasi-streamwise vortex tubes. The spanwise wavelength is found to be smaller at smaller height $y/h + 1$.

Figure 10 shows the one-dimensional spectral densities of the wall-normal velocity at $Re = 1000$, 2000, 3000, 4000, 5000. The lateral axis denotes the spanwise wavelength l and the longitudinal one is the distance $y+h$. In figure 10(a), the both axes are normalized by h. The spectral peak at $y/h + 1 = 1$ is relevant to the large-scale circulation. In the

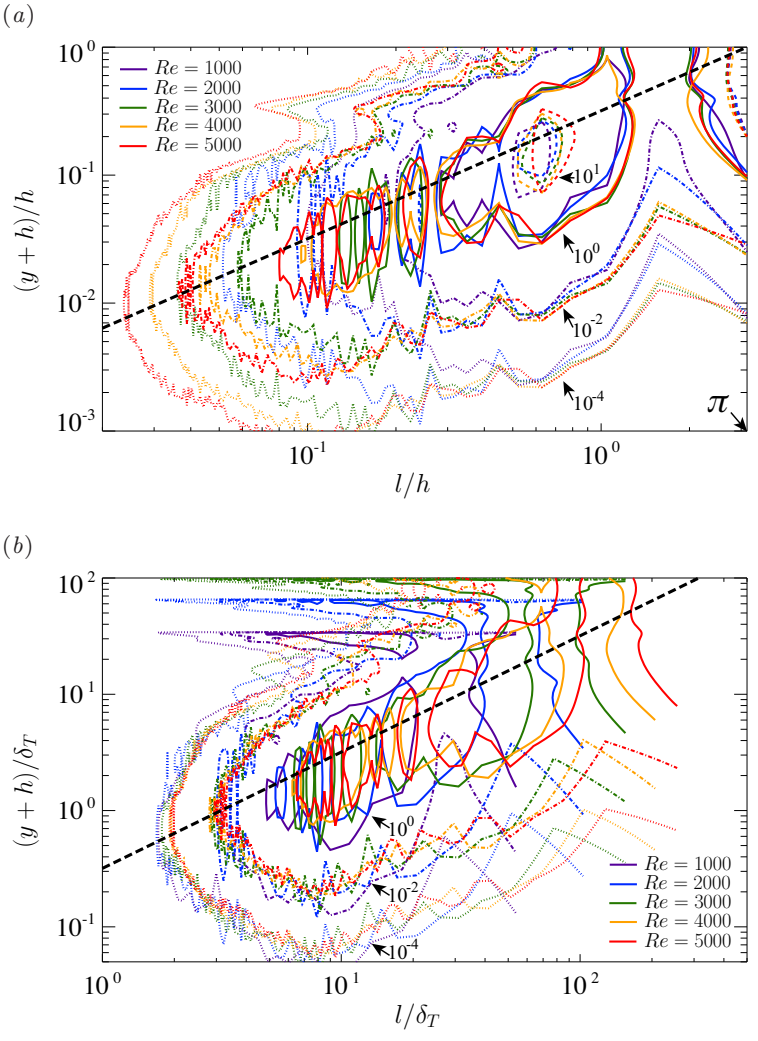

FIGURE 10. Spectral densities of the wall-normal velocity in the optimal states as a function of the spanwise wavelength l for $\lambda = 0.1$. The distance to the lower wall $y + h$ and the wavelength l are normalized by (a) the channel half width h and (b) the inner length $\delta_T = T_0/(\mathrm{d}\langle T\rangle_{xz}/\mathrm{d}y)(y = -h)$, respectively. The thick dashed line denotes $l = \pi(y + h)$.

near-wall region, $y/h + 1 \lesssim 2 \times 10^{-1}$, meanwhile, a lot of peaks are observed along the 'ridge' represented by the thick dashed line $l = \pi(y + h)$. That is to say, the near-wall quasi-streamwise vortical structures possess hierarchical self similarity. Notice that the peaks are discretely located on the ridge unlike the continuously hierarchical structure statistically observed in wall turbulence, because in a time-independent optimal field, there are no temporal fluctuations, i.e. jittering, of vortical structures. The length scale of the largest vortices scales with the outer length h, and their height is around $y/h+1 = 0.2$ regardless of Re. In figure 10(b), l and $y + h$ are normalized by the inner length

$$\delta_T = T_0 \left(\frac{\mathrm{d}\langle T\rangle_{xz}}{\mathrm{d}y}(y = -h) \right)^{-1} \tag{5.2}$$

which characterises the near-wall temperature profile. In the close vicinity of the wall,

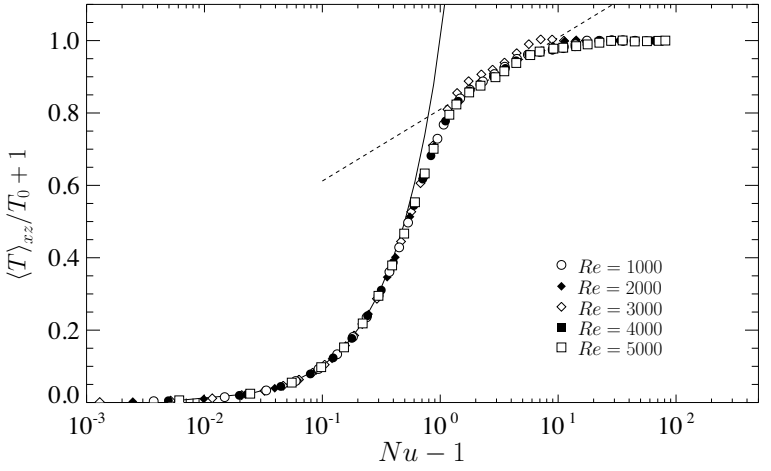

FIGURE 11. Mean temperature profile in the optimal states for $\lambda = 0.1$. The distance to the wall $y + h$ and the temperature T are normalized by the inner length and the wall temperature T_0, respectively. The solid curve and dashed line denote $\langle T\rangle_{xz}/T_0 + 1 = (y+h)/\delta_T$ and the logarithmic fit $\langle T\rangle_{xz}/T_0 + 1 = 0.086 \ln[(y + h)/\delta_T] + 0.81$ determined in the range $1 < (y + h)/\delta_T < 10$, respectively.

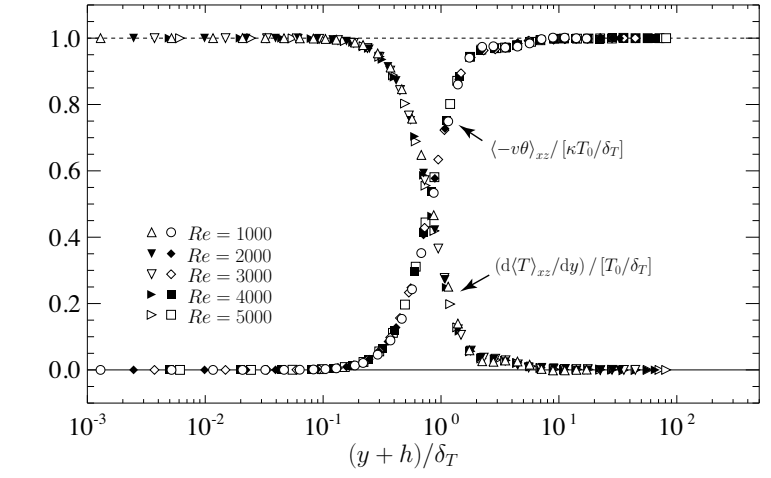

FIGURE 12. Convective and conductive heat fluxes in the optimal states as a function of the distance to the wall for $\lambda = 0.1$. The heat fluxes and the distance are normalized by the inner length.

the spectral density distribution can be seen to scale with the inner length. The vortex structures exist in the range of $\delta_T \lesssim y + h \lesssim 0.2h$ for any Re.

Figure 11 shows the mean temperature profile as a function of the distance to the wall, $(y+h)/\delta_T$. At $(y+h)/\delta_T \ll 1$, the mean temperature is expressed by $\langle T\rangle_{xz}/T_0+1 = (y+h)/\delta_T$, since thermal conduction dominants over convection (see figure 12). On the other hand, the hierarchical vortex structures lead to the logarithmic-like temperature profile in the intermediate region $1 \lesssim (y + h)/\delta_T \lesssim 10$. The dashed line represents the logarithmic fit $\langle T\rangle_{xz}/T_0+1 = 0.086 \ln[(y + h)/\delta_T]+0.81$ determined in the range $1 < (y+h)/\delta_T < 10$. It is well known that a logarithmic mean temperature profile appears as a consequence

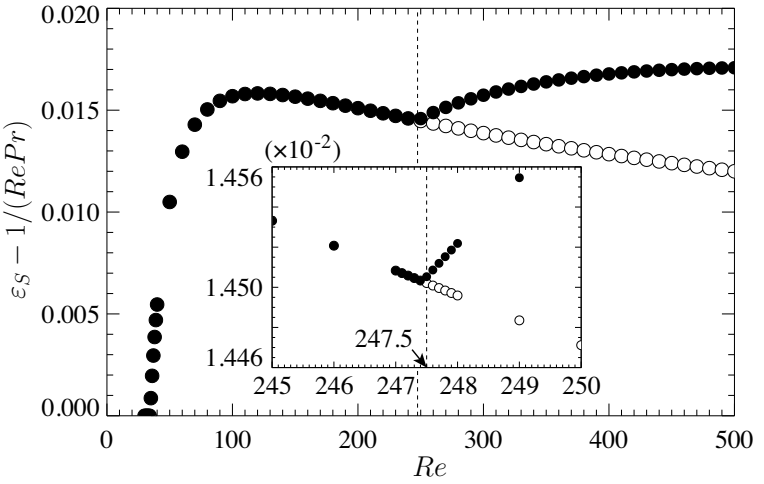

FIGURE 13. Scalar dissipation as a function of Re for $\lambda = 0.1$. Filled circles denote the scalar dissipation for the optimal state and open circles stand for that obtained from the optimisation only within a streamwise-independent two-dimensional velocity field.

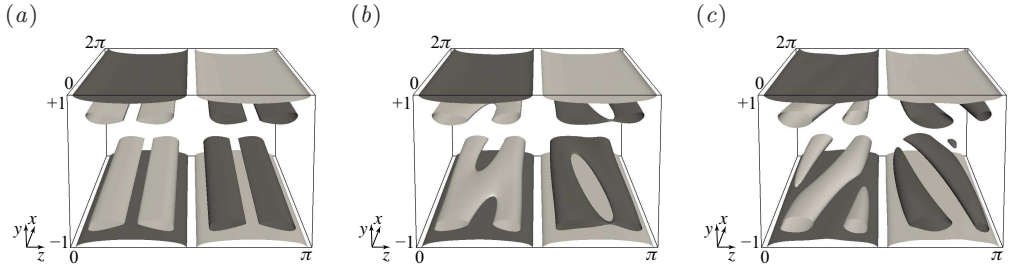

FIGURE 14. The optimal flow fields for $\lambda = 0.1$. (a) $Re = 247.4$, (b) $Re = 247.5$, (c) $Re = 249$. Light (or dark) grey objects represent isosurfaces of $\omega_x = +0.4$ (or -0.4).

of heat transfer in near-wall turbulence where self-similar hierarchical vortical structures are commonly observed. Recently the logarithmic temperature distribution has also been found numerically and experimentally in thermal convection turbulence (Ahlers *et al.* 2012, 2014). The temperature profiles are nearly uniform in the central region $y/h+1 \approx 1$ further away from the wall because of almost complete mixing of the scalar T by the large-scale circulation. The convective heat flux and the conductive heat flux are shown in figure 12. Note that the total heat flux is strictly unity at any height (see equation (2.7)). It can be seen that around $(y+h)/\delta_T \approx 1$ the two fluxes are comparable. The convective heat flux is significant at $(y+h)/\delta_T \gtrsim 1$, where the logarithmic-like mean temperature profile has been observed. At $(y+h)/\delta_T \gtrsim 10$ there is almost no contribution from the conduction, i.e. no temperature gradient.

6. Effects of flow three-dimensionality on local scalar dissipation

Figure 13 shows the scalar dissipation in the optimal state as a function of Re for $\lambda = 0.1$ to present a bifurcation diagram of the solution to the Euler–Lagrange equation. The two-dimensional solution emerges from supercritical pitchfork bifurcation on the laminar solution at $Re = 35$. The two-dimensional solution exhibits a streamwise-independent velocity field representing a pair of streamwise convection rolls shown in figure 5(a,b),

and satisfying two spatial symmetries

$$[u, v, w](x, y, z) = [u, v, -w](x, y, -z), \tag{6.1}$$

$$[u, v, w](x, y, z) = [-u, v, -w](x, -y, z). \tag{6.2}$$

As Re increases further, the secondary pitchfork bifurcation occurs on the two-dimensional solution branch at $Re = 247.5$ to create a three-dimensional solution with a shift-and-reflection symmetry

$$[u, v, w](x, y, z) = [u, v, -w](x + L_x/2, y, -z), \tag{6.3}$$

and the symmetry (6.2), which brings about the significantly higher scalar dissipation. When λ is changed, the corresponding bifurcation arises at different values of Re, but the qualitative characteristics of the bifurcation diagram is not changed (the pitchfork bifurcation occurs at larger Re as λ increases). Figure 14 shows the isosurface of the streamwise vorticity ω_x at the Reynolds numbers close to the onset of the three-dimensional solution, $Re = 247.4$, 247.5 and 249. As shown in figure 6, the optimal state has the streamwise large-scale circulation rolls. They generate sheet-like distribution of strong vorticity on the walls due to the no-slip condition, and just above the sheets the opposite-signed tube-like (or ribbon-like) streamwise vortices appear. At $Re = 247.5$, the near-wall tubular structures exhibit streamwise dependence, that is three-dimensionality. At $Re = 249$ tubular vortices bear spanwise inclination as already seen in figure 5(*c,d*) at higher Re. It is important to recall that the scalar dissipation is enhanced with the appearance of the three-dimensional structures as shown in figure 13. Figure 15 visualises isosurfaces of a positive value of the second invariant of the velocity gradient tensor

$$Q = -\frac{\partial u_i}{\partial x_j}\frac{\partial u_j}{\partial x_i} \tag{6.4}$$

for the optimal state at $Re = 249$. The spanwise vorticity fluctuation $\omega_z' = \omega_z - \langle\omega_z\rangle_{xz}$ is also shown on the Q isosurfaces by greyscale. It can be seen that most of all the extracted tube-like structures exhibits $\omega_z' > 0$. That is, the vortex tubes are tilted in the spanwise direction so that they may produce the spanwise vorticity antiparallel to the vorticity of the background shear flow. In the figures, the regions with significant increase of the local dissipation from the two-dimensional solution at the same value of Re are also shown. The local scalar and energy dissipation are given respectively by

$$D_S = \frac{1}{RePr}\left(\frac{\partial T}{\partial x_j}\right)^2, \quad D_E = \frac{1}{Re}\left(\frac{\partial u_i}{\partial x_j}\right)^2, \tag{6.5}$$

and thus it follows that $\langle D_S\rangle_{xyz} = \varepsilon_S$ and $\langle D_E\rangle_{xyz} = \varepsilon_E$. In figure 15, the regions of $D_E - D_E^{2\mathrm{D}} > 0$ are found to appear just below the vortex tubes which are flanked with the regions of $D_S - D_S^{2\mathrm{D}} > 0$, where the superscript 2D means the two-dimensional solution.

The mechanism responsible for the increase in the local scalar dissipation in the flanks of the tilted quasi-streamwise vortex tube can be explained in terms of the following simple model. Figure 16 shows illustrations of the scalar field around a vortex tube in shear flow. Suppose that the vortex tube is inclined at an angle α from the streamwise (X-) direction on the plane $Y = 0$. If $\alpha > 0$ (or $\alpha < 0$), the vortex has the spanwise (Z-) vorticity component with the same (or opposite) sign as that of the shear flow. Hereafter, the tilted vortex tubes of the same (or opposite) signed spanwise vorticity as that of the shear flow is referred to as a cyclonic (or anticyclonic) vortex. Figures 16(*d,e,f*) show the isocontours of the scalar in the $(\check{Y}, \check{Z})$-plane normal to the central axis of the vortex tube. As illustrated in these figures, the vortex tube spirally wraps the

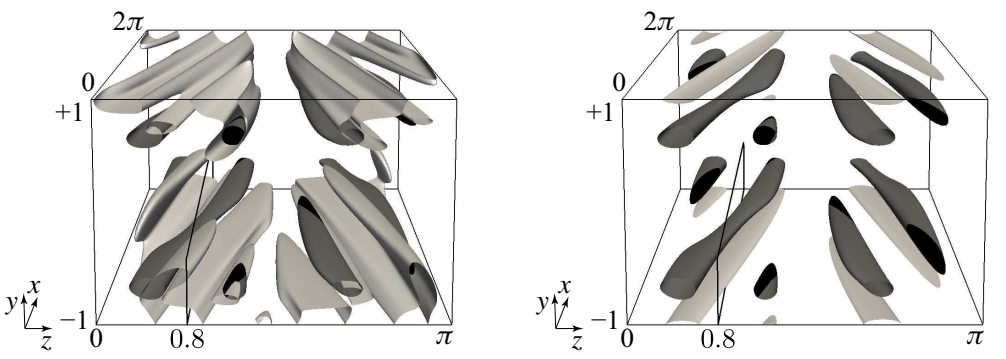

FIGURE 15. Vortical structures and significant increases in the local scalar and energy dissipation for the three-dimensional optimal velocity field against the two-dimensional optimal velocity field at $Re = 249$ for $\lambda = 0.1$. The dark grey (or black) objects represent isosurfaces, $Q = +0.03$, of the second invariant of velocity gradient tensor, on which the positive (or negative) spanwise vorticity fluctuation ω_z' are shown. Light grey objects indicate isosurfaces of (a) an increase in the local scalar dissipation, $D_S - D_S^{2D} = +0.001$, (b) an increase in the local energy dissipation, $D_E - D_E^{2D} = +0.001$. The frame in the figures indicates the plane $z = 0.8$.

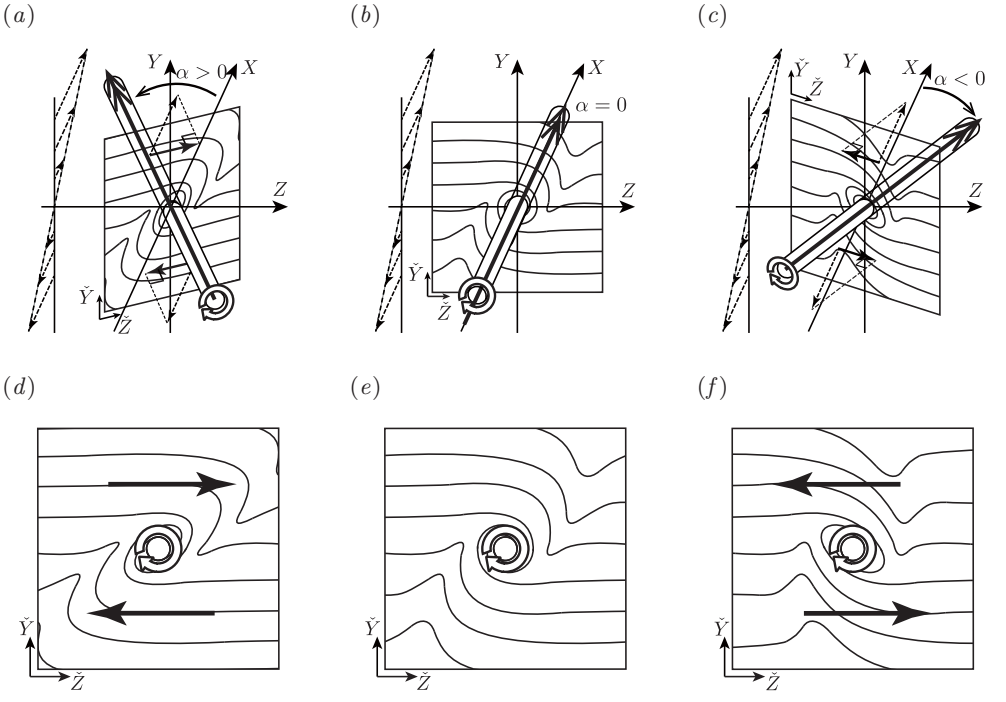

FIGURE 16. Illustration of scalar fields around cyclonic, neutral and ani-cyclonic vortex tubes in shear flow. (a,b,c) Configuration of the vortex tube in the shear flow. The vortex tube is inclined at an angle α from the X-axis on the plane $Y = 0$. (d,e,f) Isocontours of the scalar in the $(\check{Z},\check{Y})$-plane normal to the central axis of the vortex tube. (a,d) the cyclonic case $(\alpha > 0)$, (b,e) the neutral case $(\alpha = 0)$, (c,f) the anticyclonic case $(\alpha < 0)$.

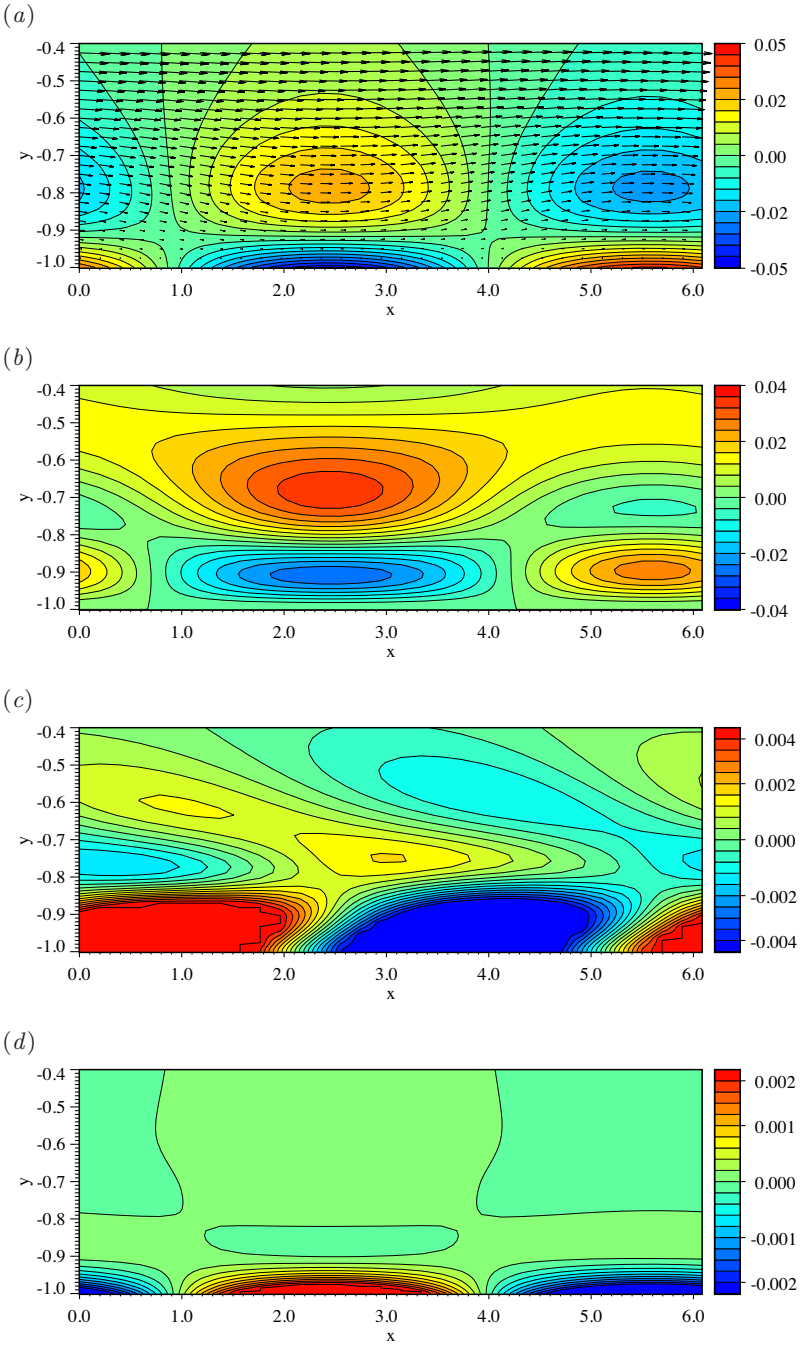

FIGURE 17. (Colour online) Two-dimensional cuts of the vorticity field, the velocity field, and the local scalar and energy dissipation fields at $Re = 249$ for $\lambda = 0.1$ at $z = 0.8$. (a) Isocontours of the spanwise vorticity fluctuation ω_z' and the velocity vectors $(u + 1, v)$ relative to the lower moving wall in the plane $z = 0.8$ shown in figure 15. (b) Isocontours of the second invariant of velocity gradient tensor Q, (c) a difference in the local scalar dissipation $D_S - D_S^{2D}$, (d) a difference in the local energy dissipation $D_E - D_E^{2D}$ in the plane $z = 0.8$.

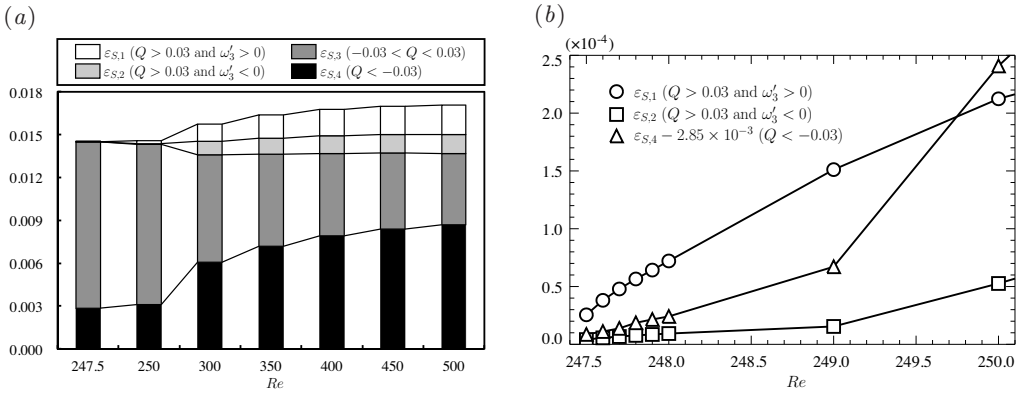

FIGURE 18. Contributions from the four regions distinguished by the second invariant of the velocity gradient tensor Q and the spanwise vorticity fluctuation ω_z' to the total scalar dissipation for $\lambda = 0.1$. Note that in (b), $\varepsilon_{S,4} - 2.85 \times 10^{-3}$ is shown instead of $\varepsilon_{S,4}$.

isosurfaces of the scalar around itself through the convective transfer induced by swirling flow. For $\alpha = 0$ (figure 16b,e), the shear flow has no effect on the scalar field because it is tangent to the scalar isosurfaces everywhere. In the case of $\alpha \neq 0$, however, the shear flow has the normal velocity component to the isosurfaces, and so it will play a distinct role in the convective scalar transfer depending on the sign of the inclination angle α. When $\alpha > 0$ (i.e., the cyclonic inclination), the spacing of the wrapped isosurfaces of the scalar is widened by the cross-axial velocity component of the shear flow as shown in figure 16(a,d). As a result, the local scalar gradient is decreased around the vortex tube, and thus the scalar dissipation is reduced. On the other hand, when $\alpha < 0$ (i.e., the anticyclonic inclination), the spacing of the wrapped isosurfaces is tightened as shown in figure 16(c,f). It turns out that the scalar dissipation is locally intensified in the flanks of the anticyclonic vortex tubes, which have been observed in the optimal states at high Reynolds numbers. Note that although the scalar dissipation is enhanced in the lower left and upper right of the anticyclone in the above simple model (figure 16d), in reality the higher scalar dissipation is observed in the lower position of the anticyclone, where the mean scalar gradient is much larger than in the upper position.

Appendix B analytically demonstrates this local effect of the anticyclonic inclination on the total scalar dissipation (or equivalently the wall heat flux in plane Couette flow) for a tilted diffusing vortex tube with circulation $\Gamma(> 0)$ in uniform shear flow of a shear rate $S(> 0)$. In this flow system the total scalar dissipation ε_S^* at early time $St|\alpha| \ll 1$ and high vortex Péclet number $\Gamma/\kappa \gg 1$ is evaluated analytically as

$$\varepsilon_S^* \approx \varepsilon_S^*|_{\alpha=0} - \alpha \left[\frac{1}{4} \kappa S^3 \Gamma \ln \left(\frac{\Gamma}{2\pi\kappa} \right) t^2 \right], \tag{6.6}$$

where the leading-order term in the right-hand side represents the total scalar dissipation for a purely aligned vortex with the shear flow ($\alpha = 0$). For the cyclonic case $\alpha > 0$ (or the anticyclonic case $\alpha < 0$), the total scalar dissipation is reduced (or enhanced) in comparison with that of the neutral case of $\alpha = 0$. This result has been obtained for self-similar diffusing vortex free from the presence of a wall; however, the essential physical mechanism proposed in figure 16 is thought to be valid even for the time-independent optimal state in a plane channel.

Besides, the near-wall vortex tube of the anticyclonic inclination has another role in heat transfer enhancement, which will be more significant at higher Reynolds numbers. Figure 17(a–d) respectively show the isocontours of ω_z', Q, $D_S - D_S^{2D}$ and $D_E - D_E^{2D}$ at

$Re = 249$. In figure 17(a) are shown the velocity vectors relative to the lower wall in the (x, y)-plane. The anticyclonic vortex of $\omega_z' > 0$ is found around $(x, y) = (2.4, -0.7)$. In figure 17(c), the higher scalar dissipation can be observed in the downstream (or right-hand-side) flank of the vortex. This local enhancement of D_S is attributed to the above-described tightening of wrapped isotherms by the cross-axial shear flow just downstream (larger x) of the anticyclonic vortex. On the other hand, the anticyclonic vortex induces the downward flow towards the lower wall upstream of (or in the left-hand side of) the vortex. The symmetric counterpart of this near-wall vortex exists on the upper wall as well. The high- (or low-) temperature fluid is pushed on the lower cold (or upper hot) wall by the near-wall anticyclonic vortex, leading to a large temperature gradient near the walls. As a result, the local scalar dissipation is significantly increased near the wall upstream of the anticyclonic vortices. The distribution of D_E is much differ from D_S (cf. figure 17c,d). The local energy dissipation is significantly increased just below the anticyclonic vortex due to the no-slip boundary condition.

Figure 18 shows the fractional contribution to the total scalar dissipation. Each contribution represents the integration over one of the separated four regions by using Q and ω_z', defined as

$$\varepsilon_{S,n} = \frac{1}{RePrV} \int_{\Omega_n} \left(\frac{\partial \theta}{\partial x_j} \right)^2 \mathrm{d}V \qquad (n = 1, 2, 3, 4), \tag{6.7}$$

where Ω_1, Ω_2, Ω_3 and Ω_4 denote the anticyclonic region of $Q > 0.03$ and $\omega_z' > 0$, the cyclonic region of $Q > 0.03$ and $\omega_z' < 0$, the shear region with $|Q| < 0.03$ (i.e. comparable vorticity and strain), and the strain region of $Q < -0.03$, respectively. Note that $\varepsilon_S = \varepsilon_{S,1} + \varepsilon_{S,2} + \varepsilon_{S,3} + \varepsilon_{S,4} + 1/(RePr)$. $\varepsilon_{S,3}$ is dominant at $Re = 247.5$ and $Re = 250$ (figure18a). The main contributor to $\varepsilon_{S,3}$ is the near-wall 'impinging jet' in between the large-scale circulation rolls, which significantly increases the heat flux on the walls as in the case of thermal convection. This contribution is, however, decreased as Re increases. Immediately after the bifurcation of the three-dimensional optimal field from the two-dimensional branch, $\varepsilon_{S,1}$ and $\varepsilon_{S,4}$ are remarkably increased as shown in figure 18(b). These are consequences of the anticyclonic inclination of the streamwise vortex tubes leading to the local enhancement of the temperature gradient by the cross-axial mean shear around the anticyclonic tube as well as by the tube-induced flow towards the wall, in the vicinity of which the strong strain arises. At large Reynolds numbers $\varepsilon_{S,4}$ becomes dominant.

7. Summary and discussion

We have explored optimal heat transfer enhancement in plane Couette flow. Optimal time-independent velocity fields have been found by maximisation of an objective functional defined as the excess of a wall heat flux (total scalar dissipation) over total energy dissipation under the constraint of incompressibility of the velocity and an advection-diffusion equation for temperature. At quite a low Reynolds number $Re \sim 10^0$, an optimal state is laminar flow, but non-trivial solutions appear at a higher Reynolds number $Re \sim 10^1$. We have obtained a streamwise-independent two-dimensional field as an optimal state. The velocity field consists of large-scale circulation rolls that play a role in heat transfer enhancement with respect to laminar conductive heat transfer as in thermal convection. A three-dimensional optimal state has been observed to arise from pitchfork bifurcation on the two-dimensional branch at $Re \sim 10^2$. The three-dimensional velocity field possesses similar large-scale rolls to those in the two-dimensional solutions; however, small-scale quasi-streamwise vortex tubes appear near the walls to be tilted

in the spanwise direction from the streamwise direction. The velocity fields exhibit extremely high performance for heat transfer enhancement even at much higher Reynolds numbers $Re \sim 10^3$. In the optimal states, higher scalar dissipation (i.e. a higher wall heat flux) is achieved with less energy dissipation than the time-averaged dissipation in a corresponding turbulent state.

In the three-dimensional optimal state at high Re, the spanwise spacing of the quasi-streamwise vortex tubes near the wall is proportionate to their distance from the wall. The spacing of the largest vortices, i.e. the large-scale circulation rolls, scales with the outer length (i.e. channel half width h), and it is independent of Re. On the other hand, the spacing of the smallest vortex scales with the inner length which is given by the temperature difference and the temperature gradient on the wall. We have observed quasi-streamwise vortical structures with hierarchical self similarity up to the distance from the wall, $0.2h$. Interestingly, the hierarchical structure leads to a logarithmic-like mean temperature profile in the region in which a convective heat flux is dominant.

We have presented the two mechanisms for heat transfer enhancement in the three-dimensional optimal state in comparison to the streamwise-independent two-dimensional state. The quasi-streamwise vortex tubes incline in the opposite direction to the vorticity of the mean shear flow. This anticyclonic inclination of the vortex tubes brings about a remarkable increase in the local and thus total scalar dissipation. The isotherms wrapped around the anticyclonic vortices undergo the cross-axial mean shear, so that the spacing of the wrapped isotherms is narrower and so the temperature gradient is steeper than those around a purely streamwise (two-dimensional) vortex tube, intensifying scalar dissipation and so a wall heat flux. The high-Péclet-number and eartly-time asymptotic analysis of the simple analytical model for a tilted straight vortex tube in uniform shear flow demonstrates that the intensification of the local scalar dissipation around the vortex tube leads to an increase in total scalar dissipation. Moreover, the tilted anticyclonic vortices highly induce the flow towards the wall to push low- (or high-) temperature fluids on the hot (or cold) wall, enhancing the wall heat flux. In wall turbulence and uniformly sheared turbulence, however, streamwise vortices have often been observed to incline in the cyclonic direction rather than in the anticyclonic direction. In real heat transfer enhancement of turbulent shear flows, therefore, the introduction of an anticyclonic inclination of quasi-streamwise vortices could be new passive control strategy for heat transfer enhancement. Our preliminary study on the introduction of an anticyclonic quasi-streamwise vortex in laminar wall-bounded shear flows has confirmed significant heat transfer enhancement in comparison to that of a cyclonic or purely streamwise vortex.

Yamamoto *et al.* (2013) have observed a roughly spanwise-independent travelling-wave-like velocity field in their controlled turbulent channel flow by optimisation of the dissimilarity between heat and momentum transfer. In such a maximisation problem of the dissimilarity the Navier–Stokes equation should be taken into consideration as a constraint on the maximisation. The optimal states found in this work are the outcomes of pursuing an incompressible velocity field which achieves more wall heat flux and less energy dissipation rather than less skin friction, and therefore they are distinct from the roughly spanwise-independent dissimilar state observed by Yamamoto *et al.* (2013).

Hassanzadeh *et al.* (2014) have recently reported time-independent optimal states for two-dimensional convection between two parallel impermeable but free-slip plates of a constant temperature difference by maximising a heat flux under the three constraints: divergence-free velocity field, temperature field satisfying an advection-diffusion equation, and fixed enstrophy. They related their optimal states to the Rayleigh–Bénard convection problem, and found the scaling of the Nusselt number Nu with the Rayleigh number Ra

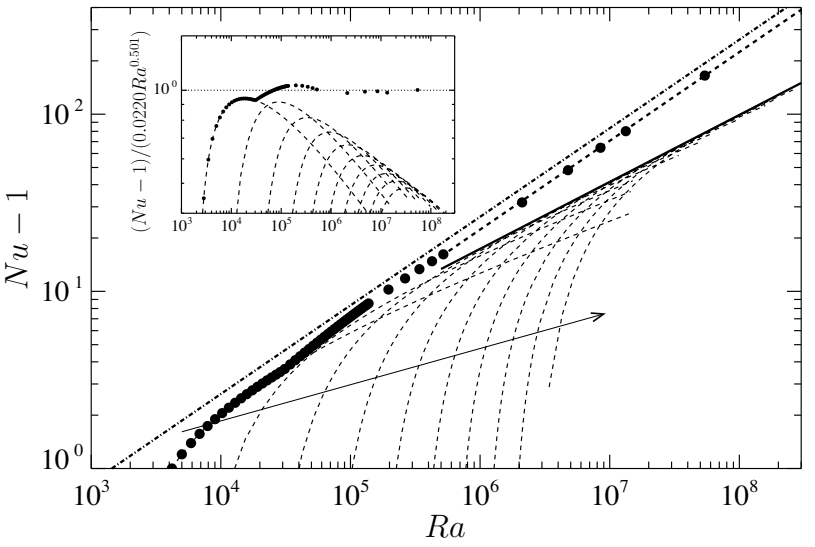

FIGURE 19. Nusselt number Nu as a function of Rayleigh number Ra. Symbolds denote the optimal state for $\lambda = 0.1$. The thick dashed line shows the power fit $Nu - 1 = 0.0220Ra^{0.501}$ determined in the range $5 \times 10^5 < Ra < 6 \times 10^7$. The dashed curves stand for the values optimised only within a streamwise-independent two-dimensional velocity field of the aspect ratio $L_z/L_y = \pi/2, \pi/4, \pi/6, \pi/8, \pi/10, \pi/12, \pi/14, \pi/16, \pi/18, \pi/20$ along the arrow. The thick solid line indicates the envelope fit $Nu-1 = 0.0937Ra^{0.378}$ determined in the range $10^7 < Ra < 10^8$. The dash-dotted line represents the upper bound in the Rayleigh–Bénard convection with the no-slip boundary condition, $Nu-1 = 0.02634Ra^{1/2}$ (Plasting & Kerswell 2003). The inset shows the compensated Nu.

as $Nu \sim Ra^{5/12}$, which agrees with the upper bounds in the case of the free-slip boundary condition, derived by the background method (Lerley *et al.* 2006; Whitehead & Doering 2012). Let us make a similar estimate for the optimal states obtained in the present study. For the combined natural and forced convection in plane Couette flow, the total energy budget equation is given by

$$8Re^3Pr^2(2\varepsilon_E - C_f) = Ra(Nu - 1). \tag{7.1}$$

By estimating Ra from ε_E, C_f and $Nu = (RePr/2)St$ in the present optimal states, we have found the scaling of Nu with Ra as $Nu-1 = 0.0220Ra^{0.501}$ for the three-dimensional optimal state at $Re = 10^3 - 10^4$, or equivalently $Ra = 5 \times 10^5 - 6 \times 10^7$ (see figure 19). The observed exponent $1/2$ of Ra is consistent with the scaling of the upper bound in the Rayleigh–Bénard convection with the no-slip boundary condition (Doering & Constantin 1996; Plasting & Kerswell 2003), and also accords with Kolmogorov's scaling law of the turbulent energy dissipation, that is $\varepsilon_E = \text{const.}$ as $Re \to \infty$. As shown in figure 8(b), the optimal state at large Re achieves nearly constant scalar and energy dissipation, and it exhibits a three-dimensional velocity field accommodating hierarchical vortical structures as discussed in §5. These results suggest that the three-dimensional velocity field with hierarchical self similarity might also lead to optimal heat transfer between two parallel no-slip plates relatively at rest under fixed energy dissipation.

Acknowledgements

We are grateful to Professor C. R. Doering at University of Michigan for useful discussions. This work was partially supported by a Grant-in-Aid Scientific Research (Grant

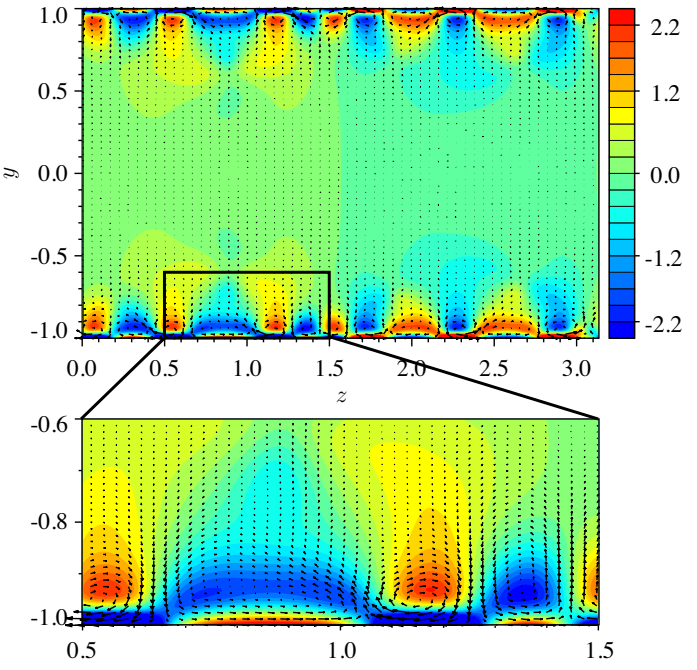

FIGURE 20. (Colour online) The cross-stream external force vectors (f_z, f_y) and the streamwise vorticity ω_x in the plane $x = 0$ for the corresponding optimal state at $Re = 1000$ for $\lambda = 0.1$.

Nos. 25249014, 26630055) from the Japanese Society for Promotion of Science (JSPS). S.M. is supported by JSPS Grant-in-Aid for JSPS Fellows Grant Number 16J00685. This research partly used computational resources under Collaborative Research Program for Young Scientists provided by Academic Center for Computing and Media Studies, Kyoto University.

Appendix A. External body force

As a consequence of the optimisation of the objective functional J, we have obtained incompressible time-independent velocity fields. The resulting velocity fields do not satisfy the Navier–Stokes equation. Thus, in order to realise the optimal state as a steady solution to the Navier–Stokes equation, we need external force. In this appendix, we estimate the external body force to discuss its characteristics.

From the steady Navier–Stokes equation, the dimensionless external body force to be added can be expressed as

$$f_i = \frac{\partial p}{\partial x_i} + u_j \frac{\partial u_i}{\partial x_j} - \frac{1}{Re} \frac{\partial^2 u_i}{\partial x_j^2} \tag{A 1}$$

in terms of the optimised velocity field $\boldsymbol{u}$. We now search for a solenoidal force field, the wall-normal component of which is null on the walls, that is $f_y(y = \pm 1) = 0$. By taking the divergence of equation (A 1), we have the Poisson equation for the pressure p,

$$\frac{\partial^2 p}{\partial x_i^2} = \frac{\partial}{\partial x_i} \left(u_j \frac{\partial u_i}{\partial x_j} \right). \tag{A 2}$$

The wall-normal component of equation (A 1) and the no-slip and impermeable condition

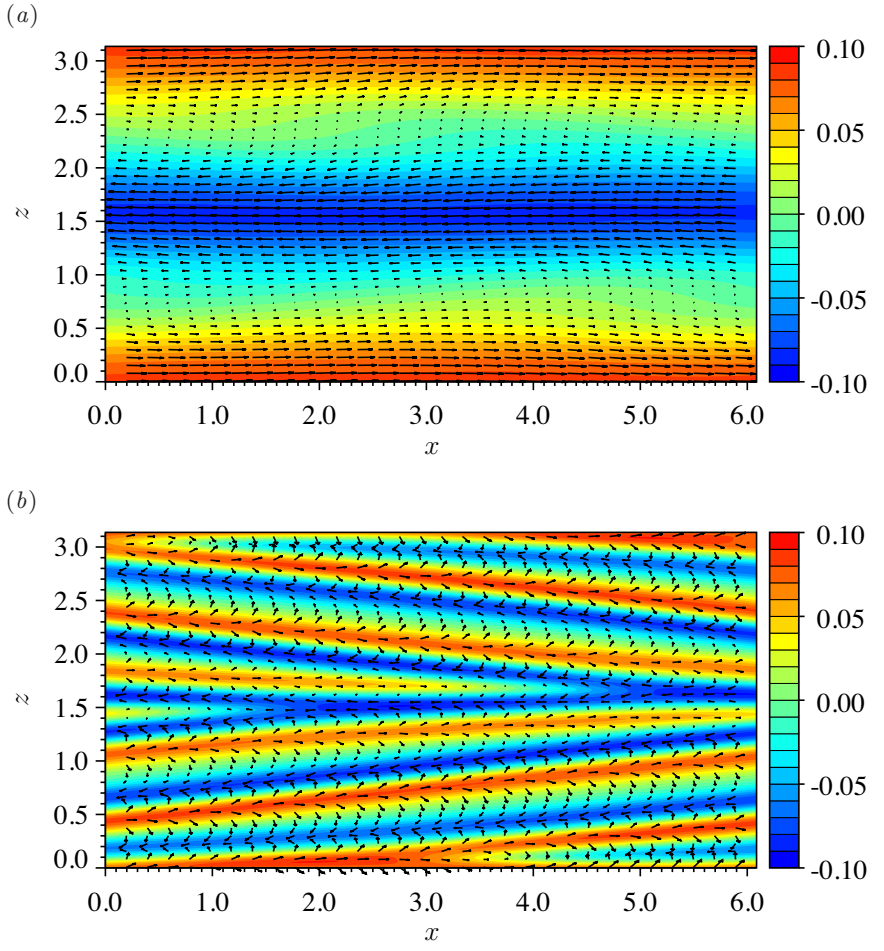

FIGURE 21. (Colour online) Spatial distribution of the wall-parallel external force and the wall-normal velocity for the corresponding optimal state at $Re = 1000$ for $\lambda = 0.1$. The wall-parallel external force vectors (f_x, f_z) and the wall-normal velocity v in the plane (a) $y = 0$, (b) $y = -0.9$.

on the walls (i.e., $\boldsymbol{u}(y = \pm 1) = 0$) yield the usual boundary condition for p on the walls $y = \pm 1$,

$$\frac{\partial p}{\partial y} = \frac{1}{Re}\frac{\partial^2 v}{\partial y^2}. \tag{A 3}$$

We obtain p as a solution to equation (A 2) supplemented by (A 3). It turns out that the external force field $\boldsymbol{f}$ can be determined by substituting $\boldsymbol{u}$ and p in equation (A 1).

Figure 20 and 21 show the cross-stream components of the external force and the streamwise vorticity for the corresponding optimal field at $Re = 1000$ for $\lambda = 0.1$. The external force appears so that it may generate small-scale streamwise vortical motion near the walls. At the same time the external force has a role in driving the large-scale circulation rolls. The streamwise external force f_x plays another important role in maintaining the steady state. It can be seen in figure 21(a) that f_x is dominant in the central region of the channel, and the sign of f_x corresponds to that of v, implying that the external force works to suppress the advection of the streamwise velocity u

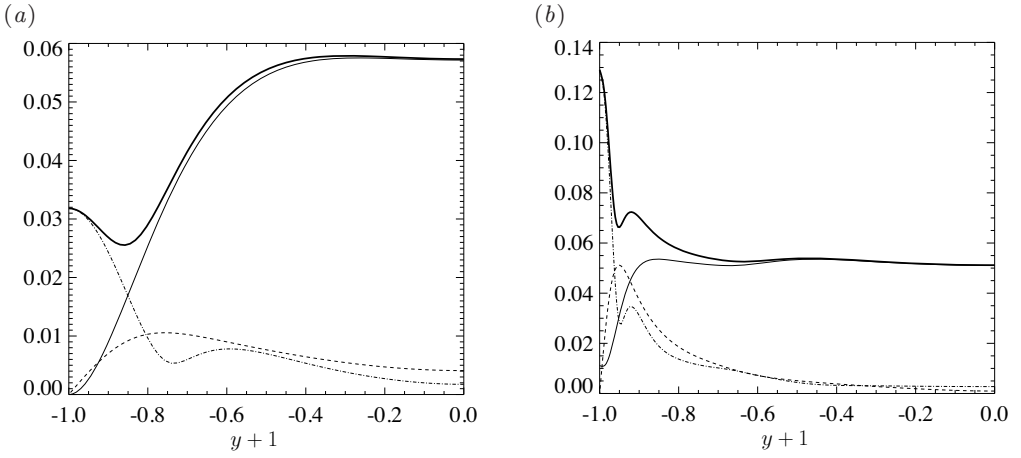

FIGURE 22. Root mean square of the external force for the corresponding optimal state as a function of the distance to the lower wall $y+1$ for $\lambda = 0.1$ at (a) $Re = 200$, (b) $Re = 1000$. ——, $\langle |\boldsymbol{f}|^2 \rangle_{xz}^{1/2}$; ——, $\langle f_x^2 \rangle_{xz}^{1/2}$; – – – –, $\langle f_y^2 \rangle_{xz}^{1/2}$; – · – · –, $\langle f_z^2 \rangle_{xz}^{1/2}$.

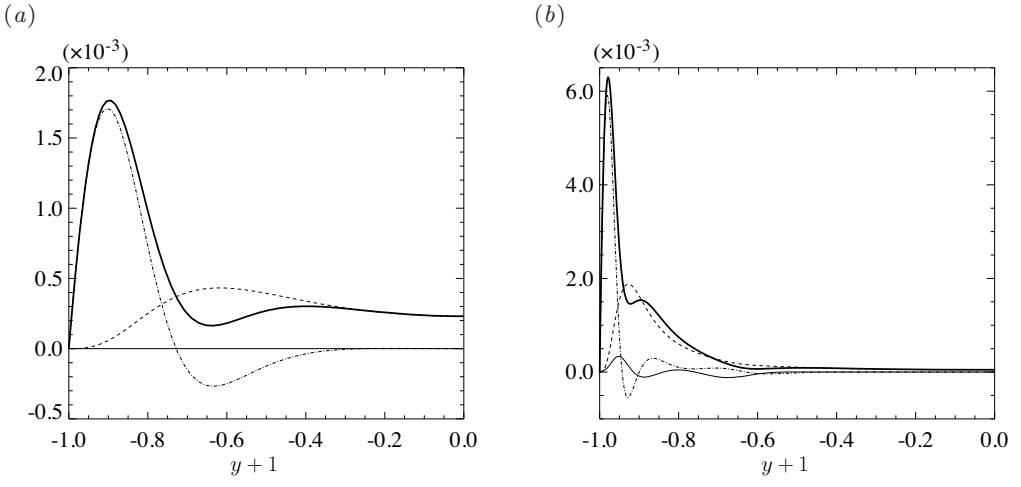

FIGURE 23. Mean energy input by the external force for the corresponding optimal state for $\lambda = 0.1$ at (a) $Re = 200$, (b) $Re = 1000$. ——, $\langle u_i f_i \rangle_{xz}$; ——, $\langle u f_x \rangle_{xz}$; – – – –, $\langle v f_y \rangle_{xz}$; – · – · –, $\langle w f_z \rangle_{xz}$.

caused by the large-scale circulation rolls. In other words, the generation of large-scale streaks is inhibited by the external force. Near the walls, the force acts each streamwise vortex (figure 21*b*). If the velocity field were to obey the Navier–Stokes equation without forcing, the vortex tube would wrap isocontours of the streamwise velocity around itself as in the wrapping of isotherms to form near-wall streaks. Thus, the vortex tubes of the anticyclonic inclination would also increase the energy dissipation in addition to the scalar dissipation by the same mechanism described in §6 (see also Kawahara 2005). The external force eliminates this wrapping effect of the streamwise velocity, and thus only the scalar dissipation is enhanced.

Figure 22 shows the root mean square of the external force as a function of the distance to the lower wall at $Re = 200$ and 1000. At $Re = 200$, the optimal state is given by a streamwise-independent two-dimensional velocity field. Note that the longitudinal axis

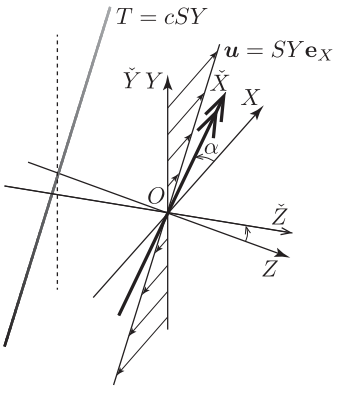

FIGURE 24. Flow configuration of the analytical model. The central axis of the vortex tube (the $\check{X}$-axis) is represented by the double arrow.

of the figure denotes the ratio of the magnitude of the external force to the inertial force U^2/h. In both cases, the spanwise component $\langle f_z^2 \rangle_{xz}^{1/2}$ is dominant near the wall. The spanwise force creates the large-scale circulation rolls and the small-scale streamwise vortices. The streamwise component is rapidly increased with the distance from the wall, and cross-streamwise force is significantly small in the central region of the channel.

The net energy input by the streamwise force can be seen to be significantly small in figure 23, which is a result of cancelling out of the energy input ($uf_x > 0$) and sink ($uf_x < 0$). In the two-dimensional optimal state at $Re = 200$, strictly $\langle uf_x \rangle_{xz} = 0$ at any height due to the flow symmetry.

Appendix B. Effects of the inclination of a straight vortex tube on scalar dissipation in uniform shear flow

Kawahara (2005) has obtained high-Reynolds-number and early-time asymptotic solutions to the incompressible Navier–Stokes equation, which represent spiral vortex layers around a straight vortex tube in uniform shear flow. His solutions have shown that the inclination of the vortex from the streamwise direction in the spanwise direction increases or decreases total energy dissipation. In this appendix, we perform a similar analysis to the problem of heat transfer around a straight vortex tube in uniform shear flow.

B.1. *Basic equations*

Let us consider temporal evolution of a passive scalar starting from an initial temperature field cSY around an infinitely straight vortex tube in uniform shear flow $SY\mathbf{e}_X$, where S (> 0) is a constant shear rate, cS is an initial uniform temperature gradient (c being a constant whose dimension is temperature/velocity), and $\mathbf{e}_X$ denotes a unit vector in the X-direction (see figure 24). The central axis of the vortex tube is on the plane $Y = 0$ and inclined at an angle α from the X-axis. We introduce the other coordinate system $O\check{X}\check{Y}\check{Z}$ given by rotating the original coordinate system $OXYZ$ at the angle α around the Y-axis. The $\check{X}$-axis corresponds to the central axis of the vortex tube.

If we suppose that the velocity, the pressure and so the temperature fields are uniform along the central axis of the tube, i.e., the $\check{X}$-axis, the velocity field $\boldsymbol{u}$ can be expressed

using the streamfunction $\psi(\check{Y},\check{Z},t)$ as

$$\boldsymbol{u} = u\mathbf{e}_{\check{X}} + \frac{\partial\psi}{\partial\check{Z}}\mathbf{e}_{\check{Y}} + \left(-\frac{\partial\psi}{\partial\check{Y}} + S\check{Y}\sin\alpha\right)\mathbf{e}_{\check{Z}}. \tag{B 1}$$

The evolution of the temperature field $T(\check{Y},\check{Z},t)$ is governed by the advection-diffusion equation

$$\left\{\frac{\partial}{\partial t} - \kappa\left(\frac{\partial}{\partial\check{Y}^2} + \frac{\partial}{\partial\check{Z}^2}\right)\right\}T - \frac{\partial(\psi,T)}{\partial(\check{Y},\check{Z})} = -S\check{Y}\sin\alpha\frac{\partial T}{\partial\check{Z}}. \tag{B 2}$$

By introducing the plane polar coordinates (r,φ) with $\check{Y} = r\cos\varphi$ and $\check{Z} = r\sin\varphi$, equation (B 2) is rewritten as

$$\left\{\frac{\partial}{\partial t} - \kappa\left(\frac{\partial^2}{\partial r^2} + \frac{1}{r}\frac{\partial}{\partial r} + \frac{1}{r^2}\frac{\partial^2}{\partial\varphi^2}\right)\right\}T - \frac{1}{r}\frac{\partial(\psi,T)}{\partial(r,\varphi)}$$
$$= -\frac{1}{2}S\sin\alpha\left(r\sin 2\varphi\frac{\partial}{\partial r} + \cos 2\varphi\frac{\partial}{\partial\varphi} + \frac{\partial}{\partial\varphi}\right)T. \tag{B 3}$$

The temperature at $r\to\infty$, far from the vortex tube, is given by

$$T = cS\check{Y}, \tag{B 4}$$

while T is assumed to be regular at $r = 0$.

In the coordinate (r,φ), the local scalar dissipation is given by

$$D_S^*(r,\varphi,t) = \kappa\left[\left(\frac{\partial T}{\partial r}\right)^2 + \frac{1}{r^2}\left(\frac{\partial T}{\partial\varphi}\right)^2\right]. \tag{B 5}$$

B.2. *High-Péclet-number asymptotic solution*

Let us compute the scalar dissipation around the diffusing vortex tube that is axisymmetric with respect to the $\check{X}$-axis as

$$\psi(r,t) = -\frac{\mathit{\Gamma}}{2\pi}\int_0^\eta \frac{1-\mathrm{e}^{-\xi^2}}{\xi}\mathrm{d}\xi, \tag{B 6}$$

where $\mathit{\Gamma}$ (>0) is the circulation, and

$$\eta = \frac{1}{2}r(\kappa t)^{-1/2} \tag{B 7}$$

is a similarity variable. Here we have supposed that $Pr = 1$ (i.e. $\nu = \kappa$). A self-similar solution to equation (B 3) for $\alpha = 0$ can be expressed as

$$T(r,\varphi,t) = cSr\mathrm{Re}[g(\eta)\mathrm{e}^{-\mathrm{i}\varphi}]. \tag{B 8}$$

Substitution of (B 6) and (B 8) into (B 3) yields

$$\frac{\mathrm{d}^2 g}{\mathrm{d}\eta^2} + \left(2\eta + \frac{3}{\eta}\right)\frac{\mathrm{d}g}{\mathrm{d}\eta} + \mathrm{i}\frac{\mathit{\Gamma}}{2\pi\kappa}\frac{1-\mathrm{e}^{-\eta^2}}{\eta^2}g = 0. \tag{B 9}$$

Boundary conditions to be imposed are that $rg(\eta)$ is regular at $\eta = 0$ and $g(\infty) = 1$. The asymptotic solution to (B 9) at high Péclet number $\mathit{\Gamma}/\kappa \gg 1$ has been obtained by Moore (1985) and Kawahara *et al.* (1997). In the far region $\eta \gg (\mathit{\Gamma}/\kappa)^{1/4}$, the solution can be written as

$$g \approx \exp\left(\mathrm{i}\frac{P_{\mathit{\Gamma}}}{4\eta^2} - \frac{P_{\mathit{\Gamma}}^2}{48\eta^6}\right), \tag{B 10}$$

where

$$P_\Gamma = \frac{\Gamma}{2\pi\kappa} \tag{B 11}$$

is the vortex Péclet number. Substituting (B 8) with the asymptotic expression (B 10) into (B 5), we have

$$D_S^* = \kappa c^2 S^2 \left[\frac{1}{2}\left|\eta\frac{\mathrm{d}g}{\mathrm{d}\eta}\right|^2 + \frac{1}{2}\eta\frac{\mathrm{d}|g|^2}{\mathrm{d}\eta} + |g|^2\right] + \kappa c^2 S^2 \mathrm{Re}\left[\eta\frac{\mathrm{d}g}{\mathrm{d}\eta}\left(g + \frac{1}{2}\eta\frac{\mathrm{d}g}{\mathrm{d}\eta}\right)\mathrm{e}^{-2\mathrm{i}\varphi}\right]. \tag{B 12}$$

Using (B 12), the total dissipation per unit axial length is evaluated as

$$\int_0^\infty \int_0^{2\pi} D_S^* r \mathrm{d}r\mathrm{d}\varphi = 8\pi\kappa^2 c^2 S^2 I_0 t, \tag{B 13}$$

where

$$I_0 = \int_0^\infty \left[\frac{1}{2}\left|\eta\frac{\mathrm{d}g}{\mathrm{d}\eta}\right|^2 + \frac{1}{2}\eta\frac{\mathrm{d}|g|^2}{\mathrm{d}\eta} + |g|^2\right]\eta\mathrm{d}\eta. \tag{B 14}$$

B.3. *Early-time asymptotic solution*

If we consider the limit of a small tilt of a vortex tube $|\alpha| \ll 1$, a solution to the advection-diffusion equation (B 3) may be written as

$$T(r,\varphi,t) = cSr[T_0(\eta,\varphi) + St\alpha T_1(\eta,\varphi) + \cdots] \tag{B 15}$$

at early time $St|\alpha| \ll 1$, where the leading-order temperature is given in a separation-of-variable form

$$T_0 = \mathrm{Re}[g(\eta)\mathrm{e}^{-\mathrm{i}\varphi}], \tag{B 16}$$

and the higher-order temperature is

$$T_1 = \mathrm{Re}\{\mathrm{i}[g_1(\eta)\mathrm{e}^{-\mathrm{i}\varphi} + g_3(\eta)\mathrm{e}^{-3\mathrm{i}\varphi}]\}. \tag{B 17}$$

By substituting (B 15) with (B 16) and (B 17) to (B 3), we obtain, for the φ-dependent part,

$$\frac{\mathrm{d}^2 g_1}{\mathrm{d}\eta^2} + \left(2\eta + \frac{3}{\eta}\right)\frac{\mathrm{d}g_1}{\mathrm{d}\eta} - 4g_1 + \mathrm{i}\frac{\Gamma}{2\pi\kappa}\frac{1-\mathrm{e}^{-\eta^2}}{\eta^2}g_1 = \zeta_1(\eta), \tag{B 18}$$

and obtain, for the 3φ-dependent part,

$$\frac{\mathrm{d}^2 g_3}{\mathrm{d}\eta^2} + \left(2\eta + \frac{3}{\eta}\right)\frac{\mathrm{d}g_3}{\mathrm{d}\eta} - 4\left(1 + \frac{2}{\eta^2}\right)g_3 + 3\mathrm{i}\frac{\Gamma}{2\pi\kappa}\frac{1-\mathrm{e}^{-\eta^2}}{\eta^2}g_3 = \zeta_3(\eta). \tag{B 19}$$

The inhomogeneous terms of (B 18) and (B 19) are given by

$$\zeta_1 = \eta\left(\frac{\mathrm{d}g}{\mathrm{d}\eta}\right)^\dagger - 4\mathrm{i}\mathrm{Im}(g), \tag{B 20}$$

$$\zeta_3 = \eta\frac{\mathrm{d}g}{\mathrm{d}\eta}, \tag{B 21}$$

where $\dagger$ denotes a complex conjugate. Boundary conditions to be imposed are that $rtg_1(\eta)$ and $rtg_3(\eta)$ are regular at $\eta = 0$, and $rtg_1(\eta) \to 0$ and $rtg_3(\eta) \to 0$ as $\eta \to \infty$. At $\eta \gg (\Gamma/\kappa)^{1/4}$, by using the asymptotic expression (B 10), ζ_1 and ζ_3 can be written,

respectively, as

$$\zeta_1 \approx \mathrm{i}\frac{P_\Gamma}{2\eta^2}\exp\left(-\mathrm{i}\frac{P_\Gamma}{4\eta^2}-\frac{P_\Gamma^2}{48\eta^6}\right)-4\mathrm{i}\sin\left(\frac{P_\Gamma}{4\eta^2}\right)\exp\left(-\frac{P_\Gamma^2}{48\eta^6}\right), \tag{B 22}$$

$$\zeta_3 \approx -\mathrm{i}\frac{P_\Gamma}{2\eta^2}\exp\left(\mathrm{i}\frac{P_\Gamma}{4\eta^2}-\frac{P_\Gamma^2}{48\eta^6}\right). \tag{B 23}$$

If we consider the far region $\eta \gg (\Gamma/\kappa)^{1/4}$, all the terms including $\mathrm{e}^{-\eta^2}$ can be neglected, and thus we can rewrite (B 18) and (B 19) as

$$\frac{\mathrm{d}^2 g_1}{\mathrm{d}\eta^2}+\left(2\eta+\frac{3}{\eta}\right)\frac{\mathrm{d}g_1}{\mathrm{d}\eta}-\left(4-\mathrm{i}\frac{\Gamma}{2\pi\kappa}\frac{1}{\eta^2}\right)g_1=\zeta_1, \tag{B 24}$$

$$\frac{\mathrm{d}^2 g_3}{\mathrm{d}\eta^2}+\left(2\eta+\frac{3}{\eta}\right)\frac{\mathrm{d}g_3}{\mathrm{d}\eta}-\left[4+\left(8-3\mathrm{i}\frac{\Gamma}{2\pi\kappa}\right)\frac{1}{\eta^2}\right]g_3=\zeta_3. \tag{B 25}$$

At large Péclet number $\Gamma/(2\pi\kappa) \gg 1$, the asymptotic solutions to (B 24) and (B 25) are given, respectively, by

$$\mathrm{Re}(g_1)=\frac{3}{4}\left[\cos\left(\frac{P_\Gamma}{4\eta^2}\right)-\frac{4\eta^2}{P_\Gamma}\sin\left(\frac{P_\Gamma}{4\eta^2}\right)\right]\exp\left(-\frac{P_\Gamma^2}{48\eta^6}\right), \tag{B 26}$$

$$\mathrm{Im}(g_1)=\frac{1}{4}\sin\left(\frac{P_\Gamma}{4\eta^2}\right)\exp\left(-\frac{P_\Gamma^2}{48\eta^6}\right), \tag{B 27}$$

$$g_3=-\left(1-\frac{\mathrm{i}\eta^2}{2P_\Gamma}\right)\exp\left(\mathrm{i}\frac{P_\Gamma}{4\eta^2}-\frac{P_\Gamma^2}{48\eta^6}\right)-\frac{\mathrm{i}\eta^2}{2P_\Gamma}\exp\left(\mathrm{i}\frac{3P_\Gamma}{4\eta^2}-\frac{3P_\Gamma^2}{16\eta^6}\right). \tag{B 28}$$

Substituting the expansion (B 15) up to the order $St|\alpha|$ with (B 16) and (B 17) into the local scalar dissipation (B 5), we have

$$\begin{aligned}
D_S^* = {} & \kappa c^2 S^2\left[\frac{1}{2}\left|\eta\frac{\mathrm{d}g}{\mathrm{d}\eta}\right|^2+\frac{1}{2}\eta\frac{\mathrm{d}|g|^2}{\mathrm{d}\eta}+|g|^2\right]+\kappa c^2 S^2\mathrm{Re}\left[\eta\frac{\mathrm{d}g}{\mathrm{d}\eta}\left(g+\frac{1}{2}\eta\frac{\mathrm{d}g}{\mathrm{d}\eta}\right)\mathrm{e}^{-2\mathrm{i}\varphi}\right] \\
& -2\kappa c^2 S^3 t\alpha\mathrm{Re}\left\{\mathrm{i}\left[\frac{1}{2}\eta^2\frac{\mathrm{d}g}{\mathrm{d}\eta}\left(\frac{\mathrm{d}g_1}{\mathrm{d}\eta}\right)^\dagger+\frac{1}{2}\eta\frac{\mathrm{d}}{\mathrm{d}\eta}(gg_1^\dagger)+gg_1^\dagger\right]\right\} \\
& +2\kappa c^2 S^3 t\alpha\mathrm{Re}\left\{\mathrm{i}\left[\frac{1}{2}\eta^2\left(\left(\frac{\mathrm{d}g}{\mathrm{d}\eta}\right)^\dagger\frac{\mathrm{d}g_3}{\mathrm{d}\eta}+\frac{\mathrm{d}g}{\mathrm{d}\eta}\frac{\mathrm{d}g_1}{\mathrm{d}\eta}\right)+\frac{1}{2}\eta\frac{\mathrm{d}}{\mathrm{d}\eta}(g^\dagger g_3+gg_1)+2g^\dagger g_3\right]\mathrm{e}^{-2\mathrm{i}\varphi}\right\} \\
& +2\kappa c^2 S^3 t\alpha\mathrm{Re}\left\{\mathrm{i}\left[\frac{1}{2}\eta^2\frac{\mathrm{d}g}{\mathrm{d}\eta}\frac{\mathrm{d}g_3}{\mathrm{d}\eta}+\frac{1}{2}\eta\frac{\mathrm{d}}{\mathrm{d}\eta}(gg_3)-gg_3\right]\mathrm{e}^{-4\mathrm{i}\varphi}\right\}.
\end{aligned} \tag{B 29}$$

From (B 29), the total scalar dissipation for $|\alpha| \ll 1$ is evaluated as

$$\int_0^\infty\int_0^{2\pi} D_S^* r\mathrm{d}r\mathrm{d}\varphi = 8\pi\kappa^2 c^2 S^2 I_0 t - 16\pi\kappa^2 c^2 S^3\alpha I_1 t^2, \tag{B 30}$$

where

$$I_1=\int_0^\infty \mathrm{Re}\left\{\mathrm{i}\left[\frac{1}{2}\eta^2\frac{\mathrm{d}g}{\mathrm{d}\eta}\left(\frac{\mathrm{d}g_1}{\mathrm{d}\eta}\right)^\dagger+\frac{1}{2}\eta\frac{\mathrm{d}}{\mathrm{d}\eta}(gg_1^\dagger)+gg_1^\dagger\right]\right\}\eta\mathrm{d}\eta. \tag{B 31}$$

At $P_\Gamma \gg 1$, using the expressions of g and g_1 given by (B 10), (B 26) and (B 27), I_1 can be written as

$$I_1 \approx \frac{P_\Gamma}{32} I_2 \tag{B 32}$$

where

$$I_2 = 3\int_0^\infty \left[-\frac{2}{\xi^2}\sin\xi + \frac{1}{\xi}(1+\cos\xi)\right] \exp\left(-\frac{\xi^3}{3P_\Gamma}\right) \mathrm{d}\xi. \tag{B 33}$$

At $P_\Gamma \gg 1$, we can estimate I_2 as

$$I_2 \approx \ln P_\Gamma, \tag{B 34}$$

which tells us that

$$I_1 \approx \frac{P_\Gamma}{32} \ln P_\Gamma. \tag{B 35}$$

Therefore, at $\Gamma/\kappa \gg 1$, we obtain the second term in the right-hand side of (B 30) as

$$-16\pi\kappa^2 c^2 S^3 \alpha I_1 t^2 \approx -\frac{1}{4}\alpha\kappa c^2 S^3 \Gamma \ln\left(\frac{\Gamma}{2\pi\kappa}\right) t^2, \tag{B 36}$$

which represents the dependence of the total scalar dissipation on the inclination of the vortex tube. When $\alpha < 0$, that is anticyclonic inclination (or $\alpha > 0$, that is cyclonic inclination), the scalar dissipation is enhanced (or reduced) in comparison with that of the neutral case of $\alpha = 0$.

REFERENCES

Ahlers, G., Bodenschatz, E., Funfschilling, D., Grossmann, S., He, X., Lohse, D., R.Stevens & Verzicco, R. 2012 Logarithmic temperature profiles in turbulent Rayleigh–Bénard convection. *Phys. Rev. Lett.* **109** (114501).

Ahlers, G., Bodenschatz, E. & He, X. 2014 Logarithmic temperature profiles of turbulent Rayleigh–Bénard convection in the classical and ultimate state for a Prandtl number of 0.8. *J. Fluid Mech.* **758**, 436–467.

Bewley, T. R., Moin, P. & Temam, R. 2001 DNS-based predictive control of turbulence: an optimal benchmark for feedback algorithms. *J. Fluid Mech.* **447**, 179–225.

Busse, F. H. 1969 On Howard's upper bound for heat transport by turbulent convection. *J. Fluid Mech.* **37**, 457–477.

Busse, F. H. 1970 Bounds for turbulent shear flow. *J. Fluid Mech.* **41**, 219–240.

Chilton, T. H. & Colburn, A. P. 1934 Mass transfer (absorption) coefficients prediction from data on heat transfer and fluid friction. *Ind. Eng. Chem.* **26**, 1183–1187.

Dipprey, D. F. & Sabersky, R. H. 1963 Heat and momentum transfer in smooth and rough tubes at various Prandtl numbers. *J. Heat and Mass Transfer* **6**, 329–353.

Doering, C. R. & Constantin, P. 1992 Energy dissipation in shear driven turbulence. *Phys. Rev. Lett.* **69**, 1648–1651.

Doering, C. R. & Constantin, P. 1994 Variational bounds on energy dissipation in incompressible flows. I. Shear flow. *Phys. Rev.* E **49** (5), 4087–4099.

Doering, C. R. & Constantin, P. 1996 Variational bounds on energy dissipation in incompressible flows. Ⅲ. Convection. *Phys. Rev.* E **53** (6), 5957–5981.

Doering, C. R., Otto, F. & Reznikoff, M. G. 2006 Bounds on vertical heat transport for infinite-Prandtl-number Rayleigh-Bénard convection. *J. Fluid Mech.* **560**, 229–241.

Hasegawa, Y. & Kasagi, N. 2011 Dissimilar control of momentum and heat transfer in a fully developed turbulent channel flow. *J. Fluid Mech.* **683**, 57–93.

Hassanzadeh, P., Chini, G. P. & Doering, C. R. 2014 Wall to wall optimal transport. *J. Fluid Mech.* **751**, 627–662.

Howard, L. N. 1963 Heat transport by turbulent convection. *J. Fluid Mech.* **17**, 405–432.

Kasagi, N., Hasegawa, Y., Fukagata, K. & Iwamoto, K. 2012 Control of turbulent transport less friction and more heat transfer. *ASME J. Heat Transfer* **134** (031009).

Kasagi, N., Suzuki, Y. & Fukagata, K. 2009 Microelectromechanical systems-based feedback control of turbulence for skin friction reduction. *Annu. Rev. Fluid Mech.* **41**, 231–251.

Kawahara, G. 2005 Energy dissipation in spiral vortex layers wrapped around a straight vortex tube. *Phys. Fluids* **17** (055111).

Kawahara, G., Kida, S., Tanaka, M. & Yanase, S. 1997 Wrap, tilt and stretch of vorticity lines around a strong thin straight vortex tube in a simple shear flow. *J. Fluid Mech.* **353**, 115–162.

Kerswell, R. R. 2001 New results in the variational approach to turbulent Boussinesq convection. *Phys. Fluids* **13**, 192–209.

Lerley, G. R., Kerswell, R. R. & Plasting, S. C. 2006 Infinite-Prandtl-number convection. Part 2. A singular limit of upper bound theory. *J. Fluid Mech.* **560**, 159–228.

Malkus, W. V. R. 1954 The heat transport and spectrum of thermal turbulence. *Proc. R. Soc. Lond.* A **225**, 196–212.

Moore, D.W. 1985 The interaction of a diffusing line vortex and an aligned shear flow. *Proc. R. Soc. London* **Ser. A 399**, 367–375.

Nicodemus, R., Grossmann, S. & Holthaus, M. 1997 Improved variational principle for bounds on energy dissipation in turbulent shear flow. *Physica* D **101**, 178–190.

Nicodemus, R., Grossmann, S. & Holthaus, M. 1998*a* The background flow method. Part 1. Constructive approach to bounds on energy dissipation. *J. Fluid Mech.* **363**, 281–300.

Nicodemus, R., Grossmann, S. & Holthaus, M. 1998*b* The background flow method. Part 2. Asymptotic theory of dissipation bounds. *J. Fluid Mech.* **363**, 301–323.

Otero, J., Wittenberg, R. W., Worthing, R. A. & Doering, C. R. 2002 Bounds on Rayleigh–Bénard convection with an imposed heat flux. *J. Fluid Mech.* **473**, 191–199.

Plasting, S. C. & Kerswell, R. R. 2003 Improved upper bound on the energy dissipation rate in plane Couette flow: the full solution to Busse's problem and the Constantin–Doering–Hopf problem with one-dimensional background field. *J. Fluid Mech.* **477**, 363–379.

Reynolds, O. 1874 On the extent and action of the heating surface of steam boilers. *Proc. Lit. Phil. Soc. Manchester* **14**, 7–12.

Robertson, J. M. & Johnson, H. F. 1970 Turbulence structure in plane Couette flow. *ASCE J. Eng. Mech. Div. Proc.* **96**, 1171–1182.

Saad, Y. & Schultz, M. H. 1986 GMRES: A generalized minimal residual algorithm for solving nonsymmetric linear systems. *SIAM J. Sci. and Stat. Comput.* **7** (3), 856–869.

Sasamori, M., Mamori, H., Iwamoto, K. & Murata, A. 2014 Experimental study on drag-reduction effect due to sinusoidal riblets in turbulent channel flow. *Exp. Fluids* **55** (1828).

Sondak, D., Smith, L. M. & Waleffe, F. 2015 Optimal heat transport solutions for Rayleigh–Bénard convection. *J. Fluid Mech.* **784**, 565–595.

Suga, K., Mori, M. & Kaneda, M. 2011 Vortex structure of turbulence over permeable walls. *Int. J. Heat and Fluid Flow* **32**, 586–595.

Townsend, A. A. 1976 *The structure of turbulent shear flow*. Cambridge University Press.

Viswanath, D. 2007 Recurrent motions within plane Couette turbulence. *J. Fluid Mech.* **580**, 339–358.

Viswanath, D. 2009 The critical layer in pipe flow at high Reynolds number. *Philos. Trans. R. Soc. A* **367**, 561–576.

Whitehead, J. P. & Doering, C. R. 2012 Rigid bounds on heat transport by a fluid between slippery boundaries. *J. Fluid Mech.* **707**, 241–259.

Yamamoto, A., Hasegawa, Y. & Kasagi, N. 2013 Optimal control of dissimilar heat and momentum transfer in a fully developed turbulent channel flow. *J. Fluid Mech.* **733**, 189–220.